Intermediate luminosity type Iax supernova 2019muj with narrow absorption lines: Long-lasting radiation associated with a possible bound remnant predicted by the weak deflagration model

Miho Kawabata [ID],[1,*] Keiichi Maeda [ID],[1] Masayuki Yamanaka [ID],[2]
Tatsuya Nakaoka,[3,4] Koji S. Kawabata [ID],[3,4,5] Kentaro Aoki,[6]
G. C. Anupama,[7] Umut Burgaz [ID],[1,8] Anirban Dutta,[7] Keisuke Isogai,[2]
Masaru Kino,[2] Naoto Kojiguchi,[1] Iida Kota,[9] Brajesh Kumar [ID],[7,10]
Daisuke Kuroda,[2] Hiroyuki Maehara [ID],[11] Kazuya Matsubayashi,[2]
Kumiko Morihana [ID],[12] Katsuhiro L. Murata,[9] Tomohito Ohshima,[13]
Masaaki Otsuka [ID],[2] Devendra K. Sahu,[7] Avinash Singh,[3,4,7]
Koji Sugitani [ID],[14] Jun Takahashi,[13] and Kengo Takagi[3]

[1]Department of Astronomy, Kyoto University, Kitashirakawa-Oiwakecho, Sakyo-ku, Kyoto, Kyoto 606-8502, Japan
[2]Okayama Observatory, Kyoto University, 3037-5 Honjo, Kamogata-cho, Asakuchi, Okayama 719-0232, Japan
[3]Hiroshima Astrophysical Science Center, Hiroshima University, 1-3-1 Kagamiyama, Higashi-Hiroshima, Hiroshima 739-8526, Japan
[4]Department of Physical Science, Hiroshima University, 1-3-1 Kagamiyama, Higashi-Hiroshima 739-8526, Japan
[5]Core Research for Energetic Universe (CORE-U), Hiroshima University, 1-3-1 Kagamiyama, Higashi-Hiroshima, Hiroshima 739-8526, Japan
[6]Subaru Telescope, National Astronomical Observatory of Japan, 650 North A'ohoku Place, Hilo, HI 96720, USA
[7]Indian Institute of Astrophysics, Koramangala 2nd Block, Bengaluru 560034, India
[8]Department of Astronomy and Space Sciences, Ege University, 35100 Izmir, Turkey
[9]Department of Physics, Tokyo Institute of Technology, 2-12-1 Ookayama, Meguro-ku, Tokyo 152-8551, Japan
[10]Aryabhatta Research Institute of Observational Sciences, Manora Peak, Nainital - 263 001, India
[11]Subaru Telescope Okayama Branch Office, National Astronomical Observatory of Japan, National Institutes of Natural Sciences, 3037-5 Honjo, Kamogata, Asakuchi, Okayama 719-0232, Japan
[12]Graduate School of Science, Nagoya University, Furo-cho, Chikusa-ku, Nagoya, Aichi 464-8602, Japan
[13]Nishi-Harima Astronomical Observatory, Center for Astronomy, University of Hyogo, 407-2 Nishigaichi, Sayo-cho, Sayo, Hyogo 679-5313, Japan
[14]Graduate School of Science, Nagoya City University, 1 Yamanohata, Mizuho-ku, Nagoya, Aichi 467-8501, Japan

Abstract

We present comprehensive spectroscopic and photometric analyses of the intermediate luminosity type Iax supernova (SN Iax) 2019muj based on multi-band datasets observed through the framework of the OISTER target-of-opportunity program. SN 2019muj exhibits almost identical characteristics to the subluminous SNe Iax 2008ha and 2010ae in terms of the observed spectral features and the light curve evolution at the early phase, except for the peak luminosity. The long-term observations unveil late-time flattening light curves as seen in luminous SN Iax 2014dt. This can be explained by the existence of an inner dense and optically thick component possibly associated with a bound white dwarf remnant left behind after the explosion. We demonstrate that the weak deflagration model with a wide range of explosion parameters can reproduce the late-phase light curves of other SNe Iax. Therefore, we conclude that a common explosion mechanism operates for different subclass SNe Iax.

Key words: supernovae: general — supernovae: individual (SN 2019muj, ASASSN-19tr, SN 2008ha, SN 2010ae, SN 2014dt)

1 Introduction

It has been widely accepted that type Ia supernovae (SNe Ia) arise from the thermonuclear runaway of a massive C+O white dwarf (WD) in a binary system. There is, however, ongoing discussion on the nature of the progenitor and the explosion mechanism; the progenitor WD may be either a Chandrasekhar-limiting-mass WD or a sub-Chandrasekhar-mass WD, and the thermonuclear runaway may be ignited near either the center or the surface of the WD (for a review, see, e.g., Maeda & Terada 2016). For SNe Ia, there is a well-established correlation between the peak luminosity and the light-curve decline rate, known as the luminosity–width relation (Phillips 1993). This relation allows SNe Ia to be used as precise standardized candles to measure the cosmic-scale distances to remote galaxies and thus the cosmological parameters (Riess et al. 1998; Perlmutter et al. 1999).

A class of peculiar SNe Ia has been discovered since the early 2000s. Their peak absolute magnitudes are significantly dimmer than those expected from the correlation. Their properties should be specified to avoid sample contamination for cosmological studies. These outliers have been called SN 2002cx-like SNe (Li et al. 2003) or SNe Iax (Foley et al. 2013). SNe Iax commonly show lower luminosities ($M_R \sim -14$ to -19 mag), lower expansion velocities (2000–8000 km s^{-1}), and lower explosion energies (10^{49}–10^{51} erg) than normal SNe Ia (e.g., Foley et al. 2009, 2013; Stritzinger et al. 2015). As an extreme example, the maximum magnitude of the faintest SN Iax, 2008ha, is only -13.74 ± 0.15 mag in the B band (Foley et al. 2009),

which is ∼4 mag fainter than the prototypical SN Iax, SN 2002cx.

Many researchers have discussed plausible models that can reproduce the wide range of the observed properties of SNe Iax (e.g., Hoeflich et al. 1995; Hoeflich & Khokhlov 1996; Nomoto et al. 1976; Jha et al. 2006; Sahu et al. 2008; Moriya et al. 2010). One such model is a weak deflagration of a Chandrasekhar-mass carbon–oxygen WD (e.g., Jordan et al. 2012; Kromer et al. 2013; Fink et al. 2014), in which a considerable part of the WD could not gain sufficient kinetic energy to exceed the binding energy, leaving a bound WD remnant after the explosion. Kromer et al. (2015) suggested, in the context of the weak deflagration model, that the faintest SNe Iax can be explained by a hybrid oxygen–neon WD with a carbon–oxygen core. While weak deflagration is a popular scenario (e.g., Jha 2017), it has not yet been established. One important test we suggest in the present work (e.g., Fox et al. 2016; Kawabata et al. 2018) is the late-time light curve behavior, which was indeed not a scope of the original light curve models by Fink et al. (2014). To consider the possible observational signature associated with the bound remnant with a range of properties, investigation of the light curves to the late phase is highly important.

To date, the number of SNe Iax for which the evolution of the late phases has been well observed remains small. The decline rates in their late phases may potentially add further diversity; they may not even correlate with the properties in the early phases (Stritzinger et al. 2015; Yamanaka et al. 2015; Kawabata et al. 2018).

SN 2019muj (ASASSN-19tr) was discovered at 17.4 mag on 2019 August 7.4 UT by the All Sky Automated Survey for SuperNovae (ASAS-SN; Shappee et al. 2014) in the nearby galaxy VV 525 (Brimacombe et al. 2019). The spectrum was obtained on August 7.8 UT by the Las Cumbres Observatory Global SN project, and this SN was classified as an SN Iax about a week before the maximum light (Hiramatsu et al. 2019). Barna et al. (2021) reported the early phase observations (∼50 d). They analyzed the spectra by comparing them with synthetic spectra obtained from radiative transfer calculations. In this paper we report the extended multi-band observation of SN Iax 2019muj, focusing especially on the analysis of its late-time light curve behavior; having been discovered in a very nearby galaxy, this SN gives us an opportunity to obtain optical and near-infrared data up to 200 d after the explosion. We describe the observations and data reduction in section 2. We present the results of the observations and compare the properties of SN 2019muj with those of other SNe Iax in section 3. SN 2019muj is classified as an intermediate SN Iax, and shows the slow evolution of the light curve at 100–200 d. In section 4 we discuss whether or not the weak deflagration can explain the observational properties of SN 2019muj. We also apply our analytical methods to other SNe Iax and demonstrate that our modified weak deflagration scenario can account for their light curves. A summary of this work is provided in section 5.

2 Observations and data reduction

We performed spectral observations of SN 2019muj using the Hiroshima One-shot Wide-field Polarimeter (HOWPol; Kawabata et al. 2008) mounted on the 1.5 m Kanata telescope of Hiroshima University, the Kyoto Okayama Optical Low-dispersion Spectrograph with an integral field unit (KOOLS-IFU; Yoshida 2005; Matsubayashi et al. 2019) on the 3.8 m Seimei telescope of Kyoto University (Kurita et al. 2020), Hanle Faint Object Spectrograph (HFOSC) mounted on the 2 m Himalayan Chandra Telescope (HCT) of the Indian Astronomical Observatory, and the Faint Object Camera and Spectrograph (FOCAS; Kashikawa et al. 2002) installed at the 8.2 m Subaru telescope, NAOJ. Multi-band imaging observations were conducted as a Target-of-Opportunity (ToO) program in the framework of the Optical and Infrared Synergetic Telescopes for Education and Research (OISTER). All the magnitudes given in this paper are in the Vega system.

2.1 Photometry

We performed *BVRI*-band imaging observations using HOWPol and *VRI*-band imaging observations using the

Hiroshima Optical and Near-InfraRed camera (HONIR; Akitaya et al. 2014) installed at the Kanata telescope. We also obtained *UBVRI*-band image data with the 2 m HCT. Additionally, *VR*-band imaging observation was performed using FOCAS installed at the Subaru telescope.

We reduced the imaging data in a standard manner for the CCD photometry. The journal of the optical photometry is listed in table 1. We adopted the point-spread function (PSF) fitting photometry method using the DAOPHOT package in IRAF.[1] We skipped the S-correction, since it is negligible for the purposes of the present study (Stritzinger et al. 2002). For the magnitude calibration, we adopted relative photometry using comparison stars taken in the same frames (figure 1). The magnitudes of the comparison stars in the *BVRI* bands were calibrated with the stars in the UGC 11860 field (Singh et al. 2018) observed on a photometric night, as shown in table 2. The secondary standard stars in this field were calibrated using the Landolt photometric standards (Landolt 1992). First-order color term correction was applied in the photometry. The amount of the correction for the color term is, for example, ∼0.03 mag in the case of HOWPol in the *B* band at the maximum light. In the longer-wavelength bands, the amount of the color term correction is smaller. While the amount of this correction varies depending on the instruments and the color of the object, it is generally negligible for the purpose of the present study.

In deriving the SN magnitudes, we did not perform the galaxy template-image subtraction method. We have checked the contamination from the host galaxy using the pre-discovery images obtained by Pan-STARRS.[2] Within an aperture of diameter ∼2″ (as a typical seeing for the Kanata observations) centered on the SN position, the background magnitudes are estimated to be $m_g = 21.58$ mag, $m_r = 21.97$ mag, or $m_i = 21.57$ mag. The contamination is thus negligible throughout the observation period. Indeed, the light curves keep declining toward the late phase, which supports that the contamination by the possible background emission is negligible. Therefore, it would not affect the conclusions in this paper.

We also performed *JHK*$_s$-band imaging observations with HONIR attached to the Kanata telescope, with the Nishi-harima Infrared Camera (NIC) installed at the Cassegrain focus of the 2.0 m Nayuta telescope at the NishiHarima Astronomical Observatory, and with the near-infrared simultaneous three-band camera (SIRIUS;

---

[1] IRAF is distributed by the National Optical Astronomy Observatory, which is operated by the Association of Universities for Research in Astronomy (AURA) under a cooperative agreement with the National Science Foundation.

[2] ⟨https://outerspace.stsci.edu/display/PANSTARRS/Pan-STARRS1+data+archive+home+page⟩.

Table 1. Log of optical observations of SN 2019muj.

Date	MJD	Phase (d)	U (mag)	B (mag)	V (mag)	R (mag)	I (mag)	Telescope (Instrument)
2019-08-08	58703.8	−3.9	—	—	17.122 ± 0.098	17.020 ± 0.111	16.932 ± 0.109	Kanata (HONIR)
2019-08-09	58704.7	−3.0	—	16.947 ± 0.075	16.911 ± 0.054	16.630 ± 0.049	16.713 ± 0.053	Kanata (HOWPol)
2019-08-09	58704.8	−2.9	—	—	16.586 ± 0.066	16.409 ± 0.085	16.421 ± 0.093	Kanata (HONIR)
2019-08-11	58706.7	−1.0	—	—	—	16.477 ± 0.023	16.467 ± 0.034	Kanata (HOWPol)
2019-08-11	58706.8	−0.9	—	—	16.471 ± 0.079	16.332 ± 0.097	16.352 ± 0.099	Kanata (HONIR)
2019-08-12	58707.7	0.0	—	—	16.173 ± 0.063	16.032 ± 0.059	15.976 ± 0.060	Kanata (HONIR)
2019-08-13	58708.7	1.1	—	—	16.507 ± 0.068	16.316 ± 0.058	16.370 ± 0.030	Kanata (HONIR)
2019-08-13	58708.8	1.1	—	16.677 ± 0.041	—	16.247 ± 0.029	16.200 ± 0.069	Kanata (HOWPol)
2019-08-30	58725.7	18.0	—	—	17.593 ± 0.036	17.158 ± 0.020	16.813 ± 0.045	Kanata (HONIR)
2019-08-30	58725.8	18.1	—	19.350 ± 0.076	17.667 ± 0.026	17.094 ± 0.055	16.803 ± 0.036	Kanata (HOWPol)
2019-09-04	58730.8	23.1	—	—	17.849 ± 0.074	17.217 ± 0.109	—	Kanata (HONIR)
2019-09-04	58730.8	23.1	—	19.396 ± 0.030	17.890 ± 0.022	17.361 ± 0.021	17.005 ± 0.032	Kanata (HOWPol)
2019-09-06	58732.7	25.1	—	19.628 ± 0.030	17.999 ± 0.024	17.442 ± 0.024	17.047 ± 0.031	Kanata (HOWPol)
2019-09-06	58732.8	25.1	—	—	17.976 ± 0.092	17.475 ± 0.095	17.165 ± 0.067	Kanata (HONIR)
2019-09-14	58740.7	33.1	—	—	18.344 ± 0.122	17.970 ± 0.146	17.487 ± 0.156	Kanata (HONIR)
2019-09-14	58740.8	33.1	—	—	—	—	17.215 ± 0.030	Kanata (HOWPol)
2019-09-15	58741.8	34.1	—	—	18.374 ± 0.186	17.803 ± 0.180	17.388 ± 0.118	Kanata (HONIR)
2019-09-15	58741.8	34.1	—	—	18.305 ± 0.051	17.750 ± 0.082	17.427 ± 0.042	Kanata (HOWPol)
2019-09-16	58742.7	35.0	—	—	18.215 ± 0.205	17.831 ± 0.128	17.425 ± 0.081	Kanata (HONIR)
2019-09-16	58742.7	35.0	—	—	18.467 ± 0.081	17.954 ± 0.034	17.427 ± 0.030	Kanata (HOWPol)
2019-09-23	58749.8	42.1	—	19.696 ± 0.012	18.461 ± 0.011	17.994 ± 0.005	17.479 ± 0.012	HCT (HFOSC)
2019-09-24	58750.6	42.9	—	19.710 ± 0.030	18.499 ± 0.059	18.018 ± 0.032	17.566 ± 0.033	Kanata (HOWPol)
2019-09-25	58751.6	43.9	—	19.848 ± 0.102	18.568 ± 0.045	18.021 ± 0.042	17.555 ± 0.066	Kanata (HOWPol)
2019-09-26	58752.7	45.0	—	20.264 ± 0.246	18.626 ± 0.028	17.957 ± 0.066	—	Kanata (HOWPol)
2019-10-01	58758.9	51.2	—	19.799 ± 0.023	18.605 ± 0.008	18.185 ± 0.010	17.730 ± 0.011	HCT (HFOSC)
2019-10-03	58759.6	51.9	—	19.954 ± 0.030	18.662 ± 0.041	18.192 ± 0.021	17.736 ± 0.031	Kanata (HOWPol)
2019-10-04	58760.7	53.0	—	20.105 ± 0.036	18.724 ± 0.029	18.224 ± 0.021	17.762 ± 0.031	Kanata (HOWPol)
2019-10-06	58762.6	55.0	—	—	18.565 ± 0.160	18.252 ± 0.106	17.816 ± 0.063	Kanata (HONIR)
2019-10-06	58762.7	55.1	—	20.271 ± 0.224	18.803 ± 0.048	18.295 ± 0.037	17.794 ± 0.049	Kanata (HOWPol)
2019-10-08	58764.6	56.9	—	—	18.644 ± 0.113	18.035 ± 0.170	17.638 ± 0.208	Kanata (HONIR)
2019-10-08	58764.7	57.0	—	20.114 ± 0.268	18.789 ± 0.039	18.297 ± 0.028	17.820 ± 0.039	Kanata (HOWPol)
2019-10-11	58767.9	60.2	—	—	18.818 ± 0.015	18.313 ± 0.010	17.899 ± 0.012	HCT (HFOSC)
2019-10-16	58772.7	65.0	—	19.727 ± 0.030	19.183 ± 0.122	18.530 ± 0.060	17.956 ± 0.056	Kanata (HOWPol)
2019-10-22	58778.6	71.0	—	—	18.801 ± 0.076	18.299 ± 0.090	17.707 ± 0.393	Kanata (HONIR)
2019-10-22	58778.6	70.9	—	20.255 ± 0.153	19.006 ± 0.029	18.547 ± 0.026	18.030 ± 0.057	Kanata (HOWPol)
2019-10-29	58785.6	77.9	—	20.254 ± 0.038	19.196 ± 0.075	18.639 ± 0.020	18.072 ± 0.035	Kanata (HOWPol)
2019-10-30	58786.9	79.2	—	—	19.085 ± 0.023	18.662 ± 0.023	18.198 ± 0.028	HCT (HFOSC)
2019-11-06	58789.7	82.0	—	20.222 ± 0.030	19.549 ± 0.020	18.715 ± 0.045	18.148 ± 0.040	Kanata (HOWPol)
2019-11-05	58792.9	85.2	—	20.100 ± 0.040	19.182 ± 0.024	18.681 ± 0.023	18.217 ± 0.032	HCT (HFOSC)
2019-11-11	58794.6	87.0	—	19.957 ± 0.030	19.610 ± 0.271	18.928 ± 0.160	18.304 ± 0.090	Kanata (HOWPol)
2019-11-25	58808.6	100.9	—	—	19.536 ± 0.058	18.944 ± 0.050	18.313 ± 0.039	Kanata (HOWPol)
2019-12-08	58825.5	117.9	—	—	19.862 ± 0.033	19.315 ± 0.035	—	Subaru (FOCAS)
2019-12-13	58830.6	122.9	—	—	19.974 ± 0.119	19.129 ± 0.048	18.381 ± 0.049	Kanata (HOWPol)
2019-12-28	58845.5	137.8	—	—	—	19.123 ± 0.042	18.470 ± 0.036	Kanata (HOWPol)
2020-02-28	58907.6	199.9	—	—	20.348 ± 0.056	19.634 ± 0.064	—	HCT (HFOSC)

Nagayama et al. 2003) installed at the 1.4 m IRSF telescope at the South African Astronomical Observatory. We adopted sky background subtraction using a template sky image obtained by dithering observation. We performed PSF fitting photometry in the same way as for the reduction of the optical data, and calibrated the magnitude using the comparison stars in the 2MASS catalog (Persson et al. 1998). We list the journal of the NIR photometry in table 3.

Additionally, we downloaded the imaging data obtained by the Swift Ultraviolet/Optical Telescope (UVOT) from the Swift Data Archive.[3] In the Swift UV data we adopted

---

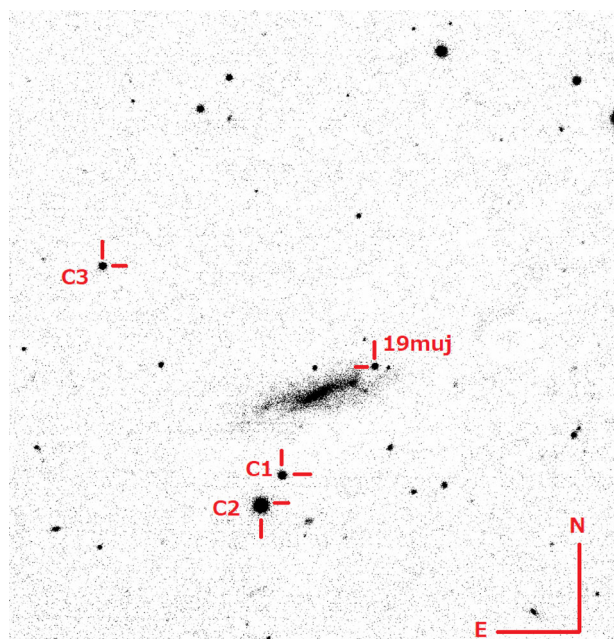[3] ⟨http://www.swift.ac.uk/swift_portal/⟩.

Fig. 1. *R*-band image of SN 2019muj and the comparison stars taken with the Kanata telescope/HOWPol on MJD 58725.76 (2019 August 30). (Color online)

absolute photometry using the zero points reported by Breeveld et al. (2011). We performed PSF fitting photometry using IRAF for these data. We list the journal of the UV photometry in table 4.

2.2 Spectroscopy

For the spectra taken with HOWPol, the wavelength coverage is 4500–9200 Å, and the wavelength resolution is $R = \lambda/\Delta\lambda \simeq 400$ at 6000 Å. For wavelength calibration, we used sky emission lines. To remove cosmic ray events, we used the L. A. Cosmic pipeline (van Dokkum 2001; van Dokkum et al. 2012). The flux of SN 2019muj was calibrated using the data of spectrophotometric standard stars taken on the same night.

The spectra with KOOLS-IFU installed on the Seimei telescope were taken through the optical fibers. We used the VPH-blue grism. The wavelength coverage is 4000–8900 Å and the wavelength resolution is $R = \lambda/\Delta\lambda \sim 500$. Data reduction was performed using the Hydra package in IRAF (Barden et al. 1994; Barden & Armandroff 1995) and reduction software specifically developed for KOOLS-IFU data. A sky frame was separately taken, which was then subtracted from the object frame. For the wavelength calibration, we used arc lamp (Hg and Ne) data.

For the spectrum obtained with FOCAS, the wavelength coverage is 3700–10000 Å and the wavelength resolution is $R = \lambda/\Delta\lambda \sim 650$ at 6000 Å. The data reduction was performed in the same way as that with HOWPol, except that

we used arc lamp (Th–Ar) data and skylines for the wavelength calibration. The journal of spectroscopy is listed in table 5.

3 Results

3.1 Light curves

Figure 2 shows the multi-band light curves of SN 2019muj, from the rising phase through the tail phase. We compare the *V*-band light curves of SN 2019muj and other SNe Iax in figure 3. We estimate the epoch of the *B*-band maximum as MJD 58707.69 ± 0.07 (2019 August 12.7) by performing a polynomial fitting to the data points around the maximum light. In this paper, we refer to the *B*-band maximum date as 0 d.

We derive the maximum magnitudes in the *B* and *V* bands as 16.623 ± 0.025 mag and 16.380 ± 0.018 mag, respectively. The distance modulus for VV525 is taken as $\mu = 32.46 \pm 0.23$ mag, which is the mean value of the results from different methods, as summarized in the NASA/IPAC Extragalactic Database (NED).[4] The extinction through the Milky Way is estimated as $E(B - V) = 0.023$ mag (Schlafly & Finkbeiner 2011), for which we adopt $R_V = 3.1$. We assume negligible extinction within the host galaxy, based on the absence of the Na D lines and the color evolution as compared with those of other SNe Iax. The *B*-band absolute peak magnitude of SN 2019muj is then −16.323 ± 0.23 mag. SN 2019muj is fainter by ∼1.5 mag than SNe 2002cx (−17.55 ± 0.34 mag, Li et al. 2003) and 2005hk (−18.02 ± 0.32 mag, Sahu et al. 2008). On the other hand, SN 2019muj is brighter than SNe Iax 2008ha (−13.74 ± 0.15 mag, Foley et al. 2009; −13.79 ± 0.14 mag, Stritzinger et al. 2014) and 2010ae (−13.44 ∼ −15.47 mag, Stritzinger et al. 2014).

We derive the decline rate of SN 2019muj in the *B* and *V* bands as $\Delta m_{15}(B) = 2.16 \pm 0.21$ mag and $\Delta m_{15}(V) = 1.18 \pm 0.04$ mag, respectively. The *B*-band decline rate is similar to SNe 2008ha (2.17 ± 0.02 mag, Foley et al. 2009; 2.03 ± 0.20 mag, Stritzinger et al. 2014) and 2010ae (2.43 ± 0.11, Stritzinger et al. 2014). This value is larger than those of the brighter SNe Iax 2002cx (1.29 ∼ 0.11 mag, Li et al. 2003) and 2005hk (1.56 ± 0.09 mag, Sahu et al. 2008).

Figure 4 shows the relationship between the peak absolute magnitude in the *V* band and the decline rate $\Delta m_{15}(V)$. The decline rate of SN 2019muj is similar to those of subluminous SNe Iax 2008ha and 2010ae. The peak magnitude is, however, between the subluminous SNe Iax and bright SNe Iax. SN 2019muj thus belongs to the intermediate

---

[4] ⟨http://ned.ipac.caltech.edu/⟩.

Table 2. Magnitudes of comparison stars of SN 2019muj.

ID	B	V	R	I	J^*	H^*	K_s^*
C1	17.258 ± 0.030	16.552 ± 0.023	16.076 ± 0.017	15.671 ± 0.031	15.206 ± 0.043	14.880 ± 0.069	14.592 ± 0.093
C2	15.426 ± 0.027	14.638 ± 0.019	14.134 ± 0.017	13.742 ± 0.030	13.294 ± 0.023	12.919 ± 0.021	12.861 ± 0.029
C3	17.786 ± 0.037	16.974 ± 0.021	16.465 ± 0.018	16.060 ± 0.030	16.369 ± 0.105	15.923 ± 0.143	15.474 ± 0.195

*The magnitudes in the NIR bands are from the 2MASS catalog (Persson et al. 1998).

Table 3. Log of NIR observations of SN 2019muj.

Date	MJD	Phase* (d)	J (mag)	H (mag)	K_s (mag)	Telescope (Instrument)
2019-08-08	58703.7	-3.9	17.228 ± 0.069	—	—	Kanata (HONIR)
2019-08-09	58704.8	-2.9	16.927 ± 0.064	17.059 ± 0.093	—	Kanata (HONIR)
2019-08-10	58705.0	-2.6	16.920 ± 0.045	16.944 ± 0.071	17.023 ± 0.108	IRSF (SIRIUS)
2019-08-11	58706.0	-1.7	16.765 ± 0.047	16.698 ± 0.075	—	IRSF (SIRIUS)
2019-08-11	58706.8	-0.9	16.661 ± 0.053	16.923 ± 0.109	—	Kanata (HONIR)
2019-08-12	58707.7	0.0	16.560 ± 0.060	16.753 ± 0.113	—	Kanata (HONIR)
2019-08-13	58708.7	1.0	16.809 ± 0.065	—	—	Kanata (HONIR)
2019-08-12	58707.8	1.1	16.443 ± 0.043	17.484 ± 0.073	—	Nayuta (NIC)
2019-08-14	58709.0	1.3	16.715 ± 0.047	16.616 ± 0.075	16.570 ± 0.114	IRSF (SIRIUS)
2019-08-16	58711.0	3.3	16.795 ± 0.045	16.567 ± 0.072	16.501 ± 0.113	IRSF (SIRIUS)
2019-08-17	58712.0	4.3	—	16.432 ± 0.083	16.526 ± 0.102	IRSF (SIRIUS)
2019-08-22	58717.0	9.3	16.981 ± 0.045	16.359 ± 0.071	16.562 ± 0.103	IRSF (SIRIUS)
2019-08-24	58719.0	11.3	17.034 ± 0.044	16.398 ± 0.070	16.648 ± 0.098	IRSF (SIRIUS)
2019-08-27	58722.0	14.3	17.072 ± 0.044	16.503 ± 0.070	17.084 ± 0.102	IRSF (SIRIUS)
2019-08-30	58725.7	18.0	—	16.405 ± 0.116	—	Kanata (HONIR)
2019-09-02	58728.0	20.3	17.329 ± 0.044	16.770 ± 0.071	17.010 ± 0.106	IRSF (SIRIUS)
2019-09-02	58728.9	21.2	17.377 ± 0.045	16.830 ± 0.071	17.141 ± 0.116	IRSF (SIRIUS)
2019-09-03	58729.9	22.2	17.401 ± 0.046	16.832 ± 0.073	—	IRSF (SIRIUS)
2019-09-04	58730.8	23.1	17.540 ± 0.113	—	—	Kanata (HONIR)
2019-09-14	58740.7	33.0	—	17.029 ± 0.142	—	Kanata (HONIR)
2019-09-15	58741.7	34.1	—	17.167 ± 0.108	—	Kanata (HONIR)
2019-09-16	58742.7	35.0	—	17.043 ± 0.166	—	Kanata (HONIR)
2019-10-08	58764.6	56.9	17.838 ± 0.174	—	—	Kanata (HONIR)
2019-10-22	58778.6	70.9	18.681 ± 0.244	18.254 ± 0.196	—	Kanata (HONIR)

*Relative to the epoch of the B-band maximum (MJD 58707.69).

**Table 4.** Log of Swift/UVOT observations of SN 2019muj.

Date	MJD	Phase* (d)	V (mag)	B (mag)	U (mag)	$uvw1$ (mag)	$uvw2$ (mag)
2019-08-07	58702.8	-4.8	17.183 ± 0.139	17.406 ± 0.078	16.212 ± 0.053	16.750 ± 0.068	17.919 ± 0.093
2019-08-08	58703.8	-3.8	16.752 ± 0.097	16.952 ± 0.060	15.885 ± 0.038	16.846 ± 0.051	17.814 ± 0.089
2019-08-09	58704.6	-3.1	16.390 ± 0.073	16.787 ± 0.048	15.752 ± 0.037	16.991 ± 0.051	—
2019-08-10	58705.4	-2.3	16.472 ± 0.078	16.641 ± 0.046	15.915 ± 0.041	17.032 ± 0.053	17.906 ± 0.074
2019-08-11	58706.8	-0.9	16.602 ± 0.090	16.537 ± 0.045	15.860 ± 0.043	17.323 ± 0.065	18.196 ± 0.103
2019-08-15	58710.7	3.0	16.470 ± 0.085	16.743 ± 0.052	16.463 ± 0.058	17.914 ± 0.086	18.662 ± 0.137
2019-08-17	58712.9	5.2	16.483 ± 0.082	16.978 ± 0.060	17.079 ± 0.080	18.417 ± 0.108	19.030 ± 0.164
2019-08-25	58720.0	12.4	17.213 ± 0.151	18.374 ± 0.176	18.663 ± 0.278	19.736 ± 0.231	19.131 ± 0.219
2019-08-29	58724.3	16.6	17.062 ± 0.160	18.407 ± 0.161	18.902 ± 0.273	—	20.414 ± 0.518
2019-09-03	58729.6	21.9	17.319 ± 0.138	18.965 ± 0.246	—	—	—
2019-09-04	58730.0	22.3	17.552 ± 0.162	18.799 ± 0.208	—	—	—

*Relative to the epoch of the B-band maximum (MJD 58707.69).

Table 5. Log of the spectroscopic observations of SN 2019muj.

Date	MJD	Phase[*] (d)	Coverage (Å)	Resolution (Å)	Telescope (Instrument)
2019-08-08	58703.7	-4.0	4000–8900	500	Seimei (KOOLS)
2019-08-10	58705.7	-2.0	4000–8900	500	Seimei (KOOLS)
2019-08-11	58706.7	-1.0	4000–8900	500	Seimei (KOOLS)
2019-08-11	58706.8	-0.9	4500–9200	400	Kanata (HOWPol)
2019-08-16	58711.7	4.1	4000–8900	500	Seimei (KOOLS)
2019-08-17	58712.7	5.0	4000–8900	500	Seimei (KOOLS)
2019-08-21	58716.7	9.0	4000–8900	500	Seimei (KOOLS)
2019-09-05	58731.7	24.0	4000–8900	500	Seimei (KOOLS)
2019-09-23	58749.8	42.1	3500–9000	300	HCT (HFOSC)
2019-09-24	58750.7	43.0	4000–8900	500	Seimei (KOOLS)
2019-09-25	58751.7	44.0	4000–8900	500	Seimei (KOOLS)
2019-09-25	58751.7	44.0	4500–9200	400	Kanata (HOWPol)
2019-10-11	58767.9	60.2	3500–9000	300	HCT (HFOSC)
2019-10-31	58787.8	80.1	3500–9000	300	HCT (HFOSC)
2019-11-06	58793.6	85.9	3500–9000	300	HCT (HFOSC)
2019-12-08	58825.5	117.8	3700–6000	650	Subaru (FOCAS)
2019-12-08	58825.5	117.8	5800–10000	650	Subaru (FOCAS)

[*]Relative to the epoch of the *B*-band maximum (MJD 58707.69).
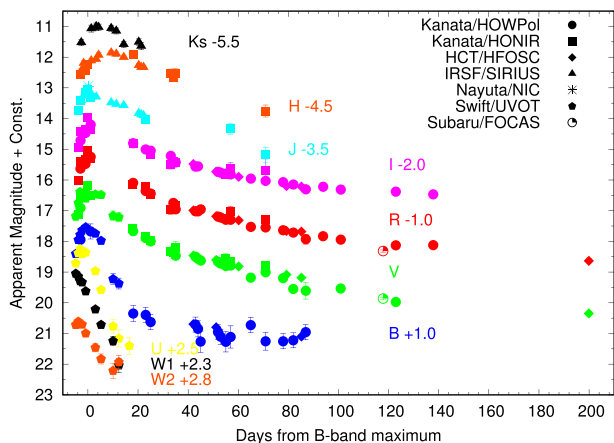
Fig. 2. Multi-band light curves of SN 2019muj. The different symbols denote data that were obtained using different instruments (see the figure legends). The light curve of each band is shifted vertically as indicated in the figure. We adopt MJD 58707.69 ± 0.07 as 0 d. (Color online)


Fig. 3. *V*-band light curve of SN 2019muj. For comparison, we plot those of SNe 2002cx (Li et al. 2003), 2005hk (Sahu et al. 2008), 2008ha (Foley et al. 2009), 2010ae (Stritzinger et al. 2014), 2011fe (Zhang et al. 2016), 2012Z (Yamanaka et al. 2015), and 2014dt (Kawabata et al. 2018). (Color online)

subclass between the bright and subluminous SNe Iax, similar to SNe 2004es and 2009J (figure 16 of Foley et al. 2013). Barna et al. (2021) also pointed out that SN 2019muj is located at the luminosity gap for SNe Iax. For the intermediate SNe Iax, multi-band data covering the rising phase are still limited. We discuss the light curve in the rising phase in subsection 4.1.

After ∼30 days, the evolution of the light curve becomes slow. The decline rates in the *V*, *R*, and *I*-band light curves between 100–200 days are calculated as 0.007 ±

0.002, 0.005 ± 0.003, and 0.004 ± 0.001 mag, respectively. We compare the light curves of SN 2019muj with those of SN 2014dt after 60 d. Their decline rates exhibit impressive similarity. In section 4 we focus on the late-phase light curves and provide analytical inspection. SN 2019muj is the second case which clearly shows a slowly evolving light curve, being consistent with the full trapping of the γ-ray energy from ^{56}Co decay (see also subsection 4.3).
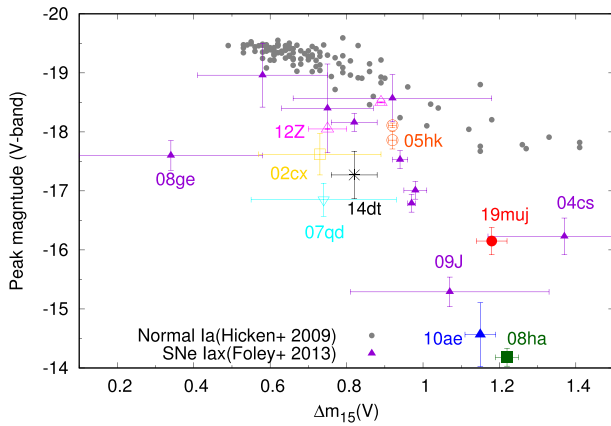
Fig. 4. Relationship of the peak absolute magnitude in the *V* band with the decline rate $\Delta m_{15}(V)$. The gray points are the data of normal SNe Ia (Hicken et al. 2009), and the other points are for SNe Iax (Li et al. 2003; Phillips et al. 2007; Sahu et al. 2008; Foley et al. 2009, 2013; McClelland et al. 2010; Stritzinger et al. 2014, 2015; Yamanaka et al. 2015; Kawabata et al. 2018). For some SNe Iax, the SN IDs are given by labels. (Color online)
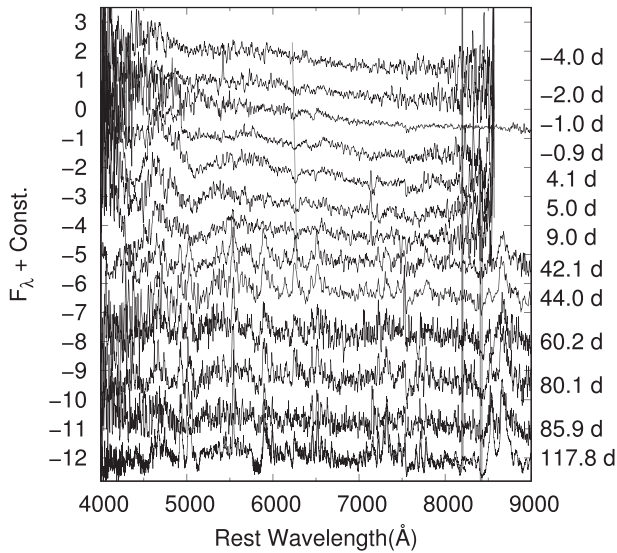

Fig. 5. Spectra evolution of SN 2019muj. The epoch of each spectrum is indicated on the right outside the panel. The gray line connects the position of the Si II λ6355 line as a function of time.

3.2 Spectral evolution

We show the optical spectra of SN 2019muj from $-4.0\,\mathrm{d}$ through $117.8\,\mathrm{d}$ in figures 5–8. In the spectra before the *B*-band maximum light, SN 2019muj shows a blue continuum with the narrow absorption lines of Si II, S II, Fe III, and C II (figures 5 and 6). Although some of the spectra of SN 2019muj are somewhat noisy, it is clearly seen that the C II absorption line is as strong as the Si II λ6355 line during the early phases. SN 2019muj is similar to SNe 2008ha and 2010ae in many spectral features (except for the Si II, Ca II IR triplet) including narrow absorption lines.
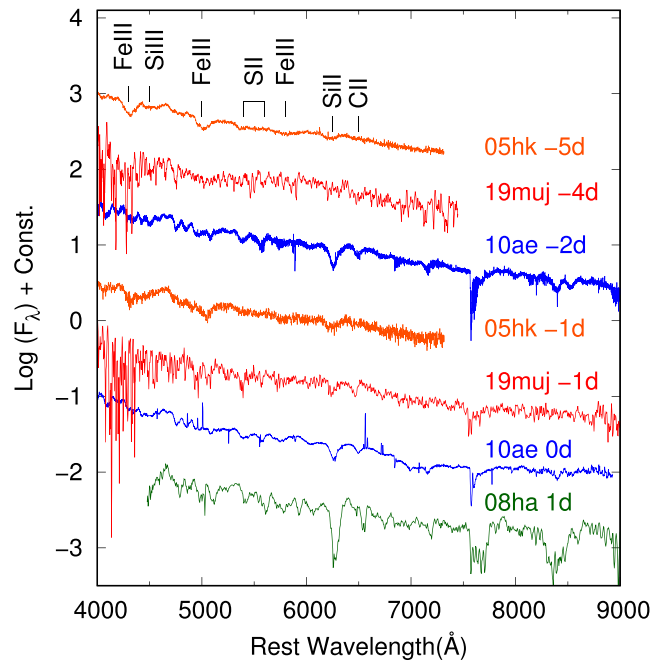
Fig. 6. Spectral comparison of SN 2019muj with other SNe Iax: 2005hk (Blondin et al. 2012), 2008ha (Valenti et al. 2009), 2010ae (Stritzinger et al. 2014). The phase of these spectra is from ~−5 d to around the maximum light. (Color online)
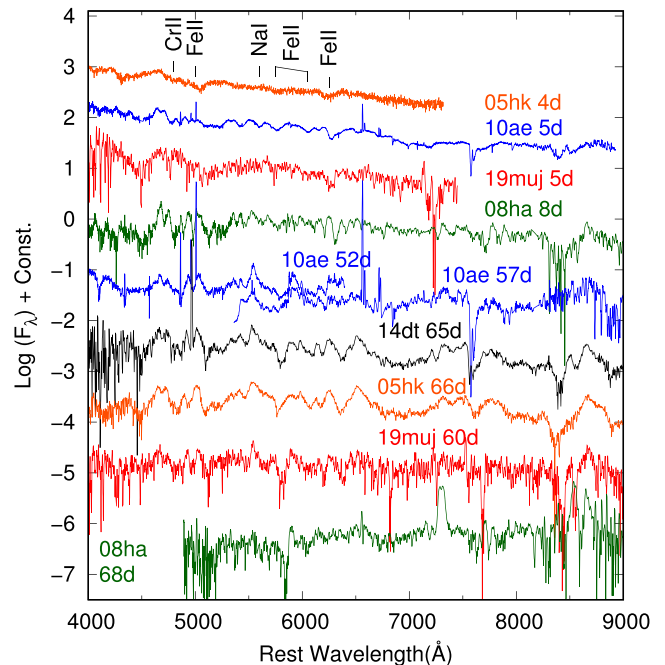
Fig. 7. Spectral comparison of SN 2019muj with other SNe Iax: 2005hk (Phillips et al. 2007; Blondin et al. 2012), 2008ha (Valenti et al. 2009; Foley et al. 2009), 2010ae (Stritzinger et al. 2014). The phase of these spectra is from ~5 to ~60 d. (Color online)

After the *B*-band maximum light, SN 2019muj shows the absorption lines of Na I D, Fe II, Fe III, Co II, and the Ca II IR triplet (figures 5 and 7). These absorption lines of SN 2019muj are narrow, similar to those seen in the
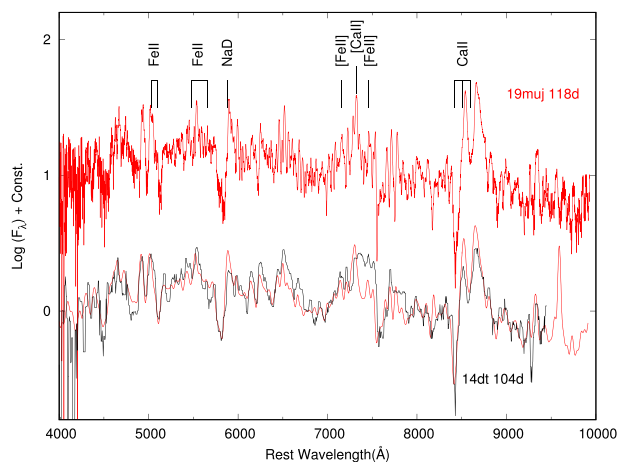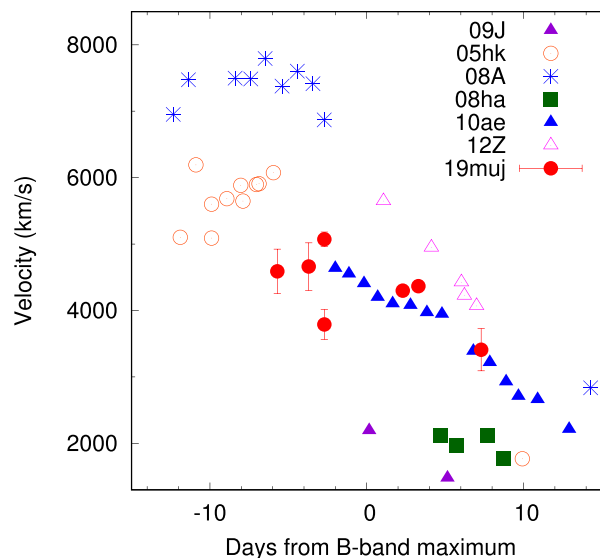
Fig. 8. Late-phase spectra of SNe 2019muj (red lines) and 2014dt (black lines; Kawabata et al. 2018). We overplot the Gaussian smoothed and blue-shifted spectrum of SN 2019muj on the spectrum of SN 2014dt. (Color online)

Fig. 9. Evolution of the line velocity of Si II λ6355 in SN 2019muj. For comparison, we plotted those for SNe 2009J, 2005hk, 2008A, 2008ha, 2010ae, and 2012Z. (Color online)

pre-maximum spectra. SN 2008ha and 2010ae have similar spectra around maximum light (see Stritzinger et al. 2014).

The late-phase spectrum (∼120 d) of SN 2019muj is plotted in figure 8. SN 2019muj shows the narrow permitted Fe II lines and several forbidden lines associated with Fe, Co, and Ca II. The line identification is based on Jha et al. (2006) and Sahu et al. (2008). In this phase, there are few comparative samples of SNe Iax. Once the spectrum of SN 2019muj is smoothed using the Gaussian function with a kernel width of 10 pixels (∼500 km s^{-1}), and then shifted to the blue by ∼900 km s^{-1} (figure 8), the similarity to SN 2014dt is striking. The spectrum of SN 2019muj in the late phase is thus characterized by low velocities, being consistent with its similarities to SN 2010ae in the earlier phase.

We obtained the line velocity of Si II λ6355 by performing a single-Gaussian fit to the absorption line profile using the splot task in *IRAF*. We determined the uncertainty as the root mean square sum of the standard deviation in the fits and the wavelength resolution. In figure 9, we show the velocity evolution of Si II λ6355. At −4.0 d the line velocity of Si II is 4590 ± 610 km s^{-1}. It is slower than that of SN 2005hk (∼6000 km s^{-1}; Phillips et al. 2007), while it is similar to SN 2010ae (∼4500 km s^{-1}; Stritzinger et al. 2014). Around maximum light, the line velocity is 4430 ± 750 km s^{-1}, which is again similar to the velocity of SN 2010ae (∼4500 km s^{-1}; Stritzinger et al. 2014). SN 2019muj has faster line velocities than faint SN 2008ha.

In summary, SN 2019muj shows the narrow lines and slow expansion velocity. Its spectroscopic features are similar to those of subluminous SNe Iax such as SNe 2008ha and 2010ae. The photometric properties of SN 2019muj

are consistent with those of the intermediate SNe Iax. Note that the spectra of the intermediate SNe Iax are similar to those of subluminous ones.

4 Discussion

SN 2019muj shows a fast decline in the early phase and narrow absorption lines similar to subluminous SNe Iax. We classify it as an intermediate-luminosity SN Iax based on its relatively bright peak magnitude. SN 2019muj is the second case which clearly shows a slow evolution of the light curve in the late phase, following bright SN Iax 2014dt (Kawabata et al. 2018). It is therefore a good target for testing the weak deflagration scenario. We also apply the analytical method to other SNe Iax, and examine whether or not their light curves can be reproduced.

4.1 Early light curves

From the light curves covering the rising phase through the peak phase, we constrain the explosion date and the rise time in the same way as Kawabata et al. (2020). We assume the homologously expanding "fireball model" (Arnett 1982; Riess et al. 1999; Nugent et al. 2011) to estimate the explosion date. In this model, the luminosity/flux (f) increases as $f \propto t^2$, where t is the time since the zero point. In this paper, we assume that the zero point in the time axis in this relation is the same for different bands (i.e., the explosion date), and adopt the same power-law index of 2 in all the *BVRI* bands.

In figure 10 we show the early *BVRI*-band light curves fitted by the fireball model with only our data. The rising
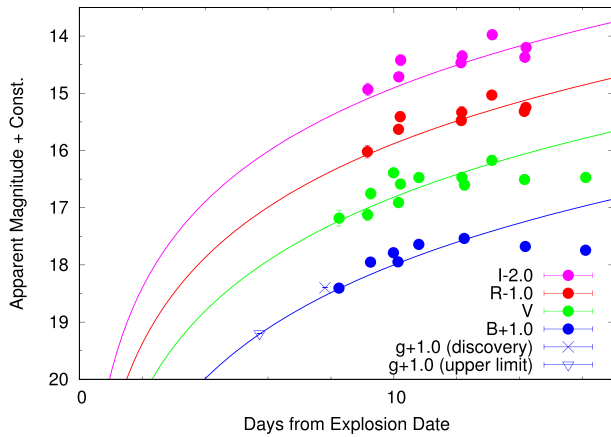
Fig. 10. Optical light curve of SN 2019muj at the early phase. We also plot the *g*-band discovery magnitude and upper-limit magnitude reported by Brimacombe et al. (2019). The explosion date is estimated to be MJD 58692.54 using the quadratic function (subsection 4.1). (Color online)

Fig. 11. Bolometric light curve of SN 2019muj. For comparison, we also plot the light curves of SNe 2002cx (Li et al. 2003), 2005hk (Sahu et al. 2008), 2008ha (Foley et al. 2009, 2010), 2011fe (Zhang et al. 2016), 2012Z (Yamanaka et al. 2015), and 2014dt (Kawabata et al. 2018). (Color online)

behavior of SN 2019muj in all the bands can be explained by this simple fireball model. Through the fitting, we estimate the explosion date as MJD 58694.59 ± 2.1. Note that the accuracy of the fit may depend on the temporal coverage of the data points used in the fit, and the error in the explosion date estimate above takes into account the change due to this effect; the final data phase included in the fit is varied by a few days. As a cross-check, we also overplotted the discovery magnitude and the non-detection, upper-limit magnitude. These ASAS-SN points, as obtained in the *g* band, were not used in the fit. Given the difference of ∼0.3 mag between the *B* and *g* bands, their points are consistent with the fireball model. No excess is found beyond the fireball prediction. However, it should be noted that there is not sufficient data in the early phase to test the light curve behavior in the first week of the explosion.

The rise time, defined as the time interval between the explosion date and the maximum date, may also provide some insights into the explosion property. Its correlations with other observational features have been investigated for normal SNe Ia (e.g., Hayden et al. 2010; Ganeshalingam et al. 2010; Jiang et al. 2020). This has also been investigated for SNe Iax (Magee et al. 2016). The rise time of SN 2019muj in the *B* band is 13.1 ± 2.1 d. Magee et al. (2016) reported a correlation between the peak absolute magnitude and the decline rate either in the *R* or *r* bands. Because of the missing data around maximum light in the *R* band, we assume that the color evolution of SN 2019muj is similar to that of other SNe Iax. Then, we convert the rising time in the *B* band to that in the *R* band. We thereby estimate the *R*-band rise time of SN 2019muj as 16–21 d. In figure 5 of Magee et al.
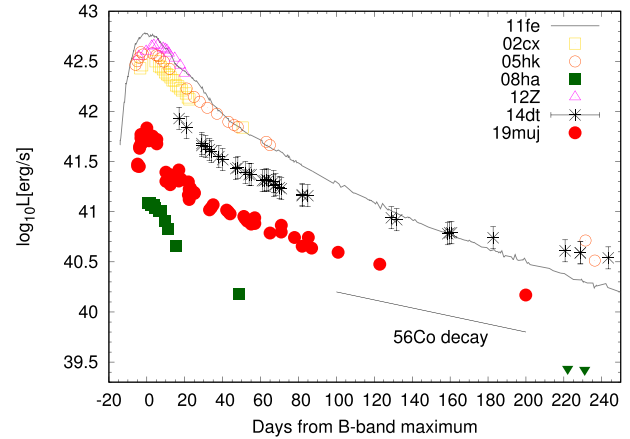
(2016), SN 2019muj is located between bright SNe Iax and subluminous ones, following the relation found by Magee et al. (2016).

4.2 Explosion parameters

We derived the bolometric luminosity of SN 2019muj by interpolating the spectral energy distribution (SED) and integrating the fluxes within the optical bands.[5] The derived bolometric light curve is shown in figure 11. SN 2019muj has intermediate luminosity among SNe Iax. With the peak luminosity and the rising time, we estimate the mass of the synthesized ^{56}Ni (Arnett 1982; Stritzinger & Leibundgut 2005) as 0.01–0.03 $M_\odot$, using the rise time and the peak bolometric luminosity as 13.1 ± 2.1 d and (0.3–0.8) × 10^{41} erg s^{-1}, respectively. The estimated ^{56}Ni mass is consistent with the value reported by Barna et al. (2021).

We then estimate M_{ej} and E_k of the ejecta of SN 2019muj by applying the scaling laws

$$t_d \propto \kappa^{1/2} M_{ej}^{3/4} E_k^{-1/4}, \tag{1}$$

$$v \propto E_k^{1/2} M_{ej}^{-1/2}, \tag{2}$$

where t_d is the diffusion timescale (around the light curve width in the early phase), κ is the absorption coefficient for optical photons, and v is the typical expansion velocity of the ejecta. Here, we calibrate the relations by the properties of the well-studied SN Ia 2011fe (Pereira et al. 2013) to anchor the normalization.[6] We then obtain

---

[5] In the bolometric luminosity, the contribution from the NIR emission is small (SN 2012Z; Yamanaka et al. 2015). Then, we estimated it using only the optical bands in this paper.

[6] The explosion parameters of SN 2011fe are $E_{k, 11fe} = 1.2 \times 10^{51}$ erg and $M_{ej, 11fe} \sim 1.4 M_\odot$.

$E_{k,19\text{muj}} \sim 0.02\text{–}0.19 \times 10^{50}$ erg, $M_{\text{ej},19\text{muj}} \sim 0.16\text{–}0.95\,M_{\odot}$, and $\kappa_{19\text{muj}}/\kappa_{11\text{fe}} \sim 0.7\text{–}4.1$ (see Kawabata et al. 2018 for details).

4.3 Comparison with the weak deflagration model

For SNe Iax, some explosion models have been proposed. Among those models is the weak deflagration model, which leaves a bound WD remnant after the explosion; in this model, changing the number of ignition spots or the initial composition of the WD can explain the observational properties from bright SNe Iax to subluminous ones like SN 2008ha (Fink et al. 2014; Kromer et al. 2015). In this section we compare the observational properties of SN 2019muj to the expectations from this particular explosion model. In the present work we focus on the light curve behavior; the spectroscopic properties have been investigated by Barna et al. (2021), who showed that the weak/failed deflagration model can roughly explain the early-phase spectral evolution, while the degree of abundance mixing found for SN 2019muj (or SNe Iax in general) is not as substantial as expected by the model.

In the model sequence of Fink et al. (2014), the models N1def, N3def, and N5def cover the explosion parameters constrained for SN 2019muj (see subsection 4.2). In figure 12 we compare the bolometric light curve of SN 2019muj and the light curves calculated for these models. The bolometric light curve of SN 2019muj is similar to that expected from the N1def model, while the
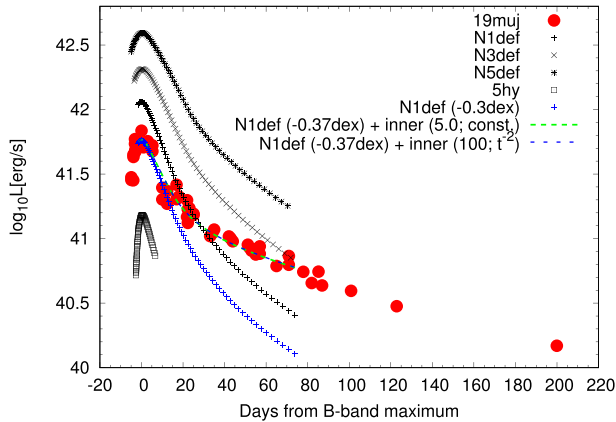
Fig. 12. Bolometric light curve of SN 2019muj. We compare the the weak deflagration model light curve (black points; Fink et al. 2014; Kromer et al. 2015), N5def, N3def, N1def, and N5hybrid, respectively. The blue points are the N1def model shifted downward to fit the peak luminosity of SN 2019muj. The green and blue dashed lines are the two-component model as the sum of the weak deflagration model and the simple radioactive-decay light curve model (see subsection 4.3); the evolution of the optical depth is taken as either $\tau = $ constant (green) or $\tau \propto t^{-2}$ (blue). (Color online)

peak luminosity of SN 2019muj is slightly fainter than the N1def model (see also Barna et al. 2021). Then, we try to match the light curve of the N1def model to that of SN 2019muj around the peak by shifting the model luminosity. This modified model can reproduce the light curve of SN 2019muj until $\sim$20 d. However, in the tail phase, SN 2019muj shows a slow decline, unlike the model light curves that fade away very quickly.

To explain the light curve in the late phase, an additional energy source is required. In the model sequence by Fink et al. (2014), they indeed predicted the presence of a bound WD remnant, which contains some ^{56}Ni. To test this hypothesis further, we first calculate the decline rate in the late phase by fitting a linear function to the bolometric light curve. The decline rate is found to be $\sim$0.004 dex d^{-1} (0.01 mag d^{-1}) over 60–210 d, which matches the expectation from nearly full trapping of the γ-rays. This indicates that the additional component is powered by the decay of ^{56}Co within a high-density inner component.

This additional contribution is not directly included in the model light curves of Fink et al. (2014). Indeed, the radiation process regarding this bound remnant has not been well understood (e.g., Foley et al. 2016). There are several possible scenarios in which the bound WD remnant would create the inner dense component: (i) It is possible that the component is indeed a static bound WD remnant itself. (ii) Alternatively, the bound WD could create the inner ejecta with a slow expansion velocity, which may behave like the additional inner dense component due to its high density. (iii) Finally, there is a possibility that a high-density wind is launched from a bound WD remnant (Foley et al. 2016).

Here, we consider a simple phenomenological model (Kawabata et al. 2018) where the power from ^{56}Ni in the bound remnant is radiated away through a dense environment (either in the static WD, slowly moving inner ejecta, or a possible wind), without much energy loss or time delay. As the bolometric luminosity in the late phase, we thus consider the simple radioactive-decay light curve model (Maeda et al. 2003):

$$L_{\text{bol}} = M(^{56}\text{Ni})_{\text{in}} \left\{ e^{(-t/8.8\,\text{d})} \epsilon_{\gamma,\text{Ni}} (1 - e^{-\tau}) \right.$$
$$\left. + e^{(-t/111\,\text{d})} \left[\epsilon_{\gamma,\text{Co}} (1 - e^{-\tau}) + \epsilon_{e^+} \right] \right\}, \quad (3)$$

where $\epsilon_{\gamma,\text{Ni}} = 3.9 \times 10^{10}$ erg s^{-1} g^{-1} is the energy deposition rate by ^{56}Ni via γ-rays, and $\epsilon_{\gamma,\text{Co}} = 6.8 \times 10^{9}$ erg s^{-1} g^{-1} and $\epsilon_{e^+} = 2.4 \times 10^{8}$ erg s^{-1} g^{-1} are those by the ^{56}Co decay via γ-rays and positron ejection. The optical depth of the inner component, τ, will evolve with time differently for the different scenarios for the inner component; this is expected to be constant for the bound WD, or to evolve as $\tau \propto t^{-2}$ for the slowly moving ejecta. These two possibilities will be
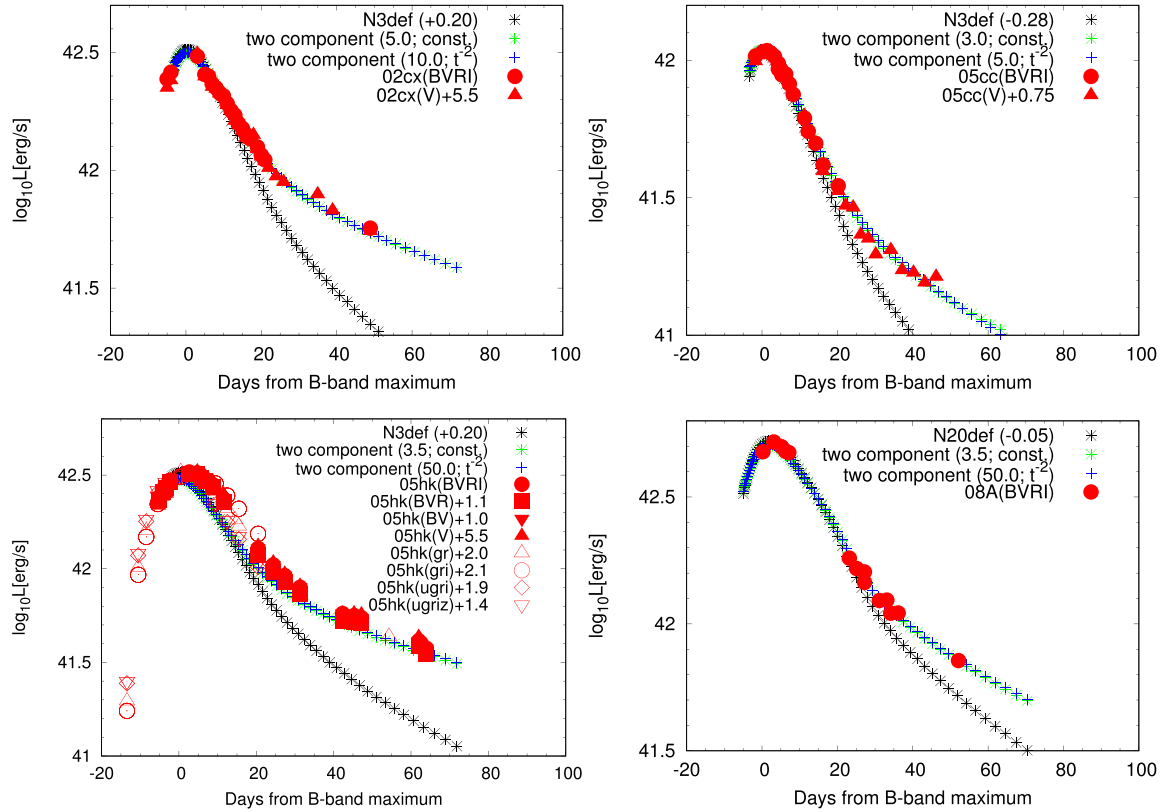
Fig. 13. Bolometric light curves of SNe Iax (red points). We compare the weak deflagration model light curve (black points; Fink et al. 2014). The black points are shifted to fit the peak luminosity of each SN Iax. The green and blue points are the two-component model as the sum of the weak deflagration model and the simple radioactive-decay light curve model (see subsection 4.3); the evolution of the optical depth is taken as either $\tau = $ constant (green) or $\tau \propto t^{-2}$ (blue). (Color online)

examined below. In the case of the WD wind, the evolution is not trivial, but it likely decreases with time as the mass-loss rate goes down; it is probably a reasonable guess that the rate of decrease for the wind case is between the two cases mentioned above. Note that $M(^{56}\mathrm{Ni})_{\mathrm{in}}$ and the optical depth here refer to those of the inner component alone without the outer component estimated in subsection 4.2.

We then add this additional component to the model light curve of Fink et al. (2014). In figure 12 we show this combined light curve model. The mass of ^{56}Ni in the inner component is derived as $\sim$0.018 $M_\odot$. For the case of constant optical depth, we have derived $\tau \sim 5.0$. τ is the lower limit, and any value larger than this does not affect the change in the bolometric luminosity. For the case of slow-moving inner ejecta, the optical depth is characterized as

$$\tau \simeq 1000 \times \left[\frac{(M_{\mathrm{ej}}/M_\odot)^2}{E_{51}}\right]_{\mathrm{in}} \left(\frac{t}{\mathrm{d}}\right)^{-2}, \qquad (4)$$

where M_{ej} is the ejecta mass, and E_{51} is the kinetic energy in 10^{51} erg (both only for the inner component). We can

reproduce the light curve with $[(M_{\mathrm{ej}}/M_\odot)^2/E_{51}]_{\mathrm{in}} \sim 100$. The analysis here indicates the existence of an inner dense component, irrespective of the specific scenarios for its origin. A high-density component in the inner part was also seen in the bright SN Iax 2014dt through similar analysis (Kawabata et al. 2018); we thus find this inner component to be a common property shared by bright and intermediate-luminosity SNe Iax.

As shown above, the light curve is well reproduced irrespective of the evolution of the optical depth. In other words, from this analytical model of the bolometric light curve, it is difficult to distinguish the scenarios for the origin of the inner component. This stems from the observed decay rate following the full trapping of the γ-rays; as long as $\tau \gg 1$, the result is not dependent on the time evolution of the optical depth. Indeed, in the model for the slowly moving ejecta, the optical depth will decrease below unity $\sim$1 yr after the explosion. Therefore, further following the light curve evolution even longer than the observation in the present work may be useful to distinguish at least the slowly moving ejecta scenario. Also, the spectral evolution in the late phase is key to addressing this question.
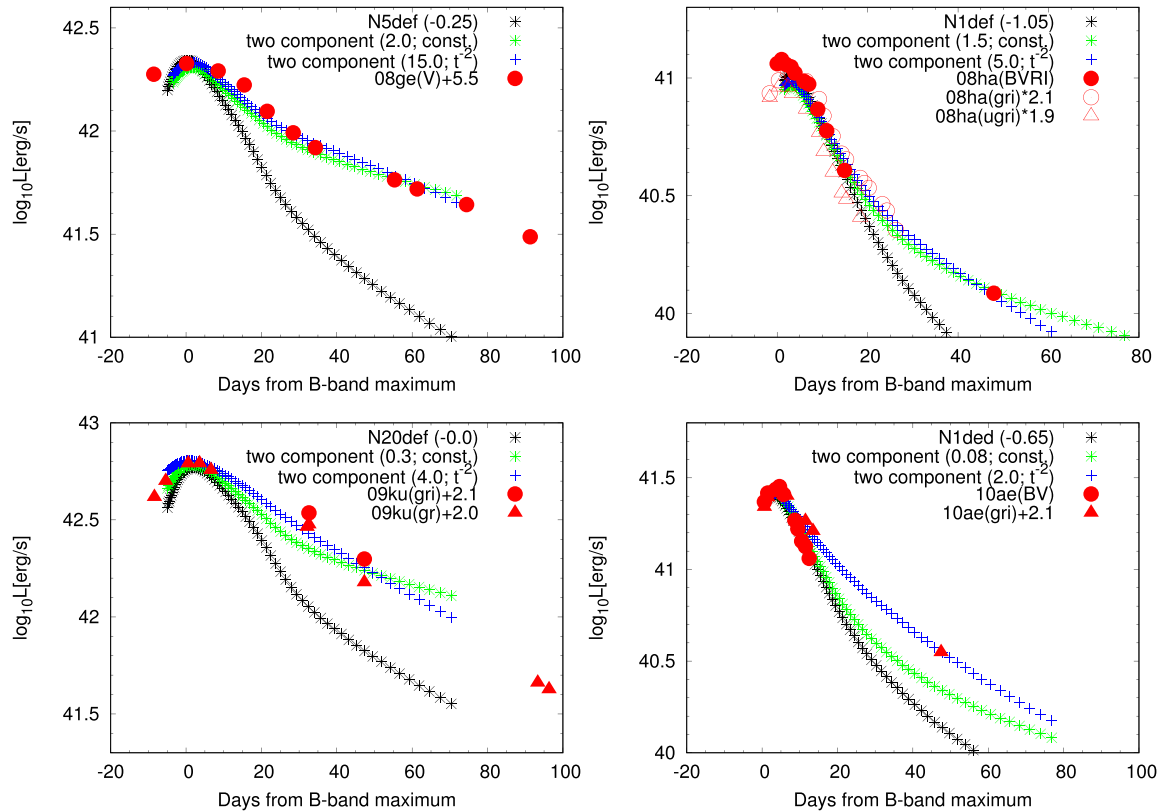
Fig. 14. As figure 13 but for different SNe Iax. (Color online)

4.4 Bound WD remnants in all SNe Iax?

In this section we expand the analysis in subsection 4.3 on the light curve behavior to a sample of SNe Iax. We estimate the bolometric luminosities of these SNe Iax using the same method as adopted for SN 2019muj (see the Appendix for further details). In figures 13, 14, 15, and 16 we compare the bolometric light curves of SNe Iax and those predicted by Fink et al. (2014) for the weak deflagration model series. We can find a subset of the model series that can fit the early-phase light curve of individual SNe Iax. However, the models cannot replicate the late-phase slow evolution seen in the observed light curves, as is similar to the case for SN 2019muj, except for SNe 2011ay and 2019gsc. Since their models do not consider the inner-part ejecta components, we further consider the light curve model with a variety of inner-part ejecta properties (see subsection 4.3) to fit the bolometric light curves of other SNe Iax. Using the same methodology as in subsection 4.3, we try to fit the combined light curve model with the two cases where τ is either constant (i.e., the static remnant) or evolves as $\tau \propto t^{-2}$ (i.e., the slowly moving inner ejecta). Their light curves are well reproduced by this model sequence (figures 13, 14, 15, and 16). Again, similarly to the case for SN 2019muj,

we unfortunately cannot constrain the time evolution of the optical depth with the available data set. This highlights the importance of observations in even later phases (subsection 4.3).

Most SNe Ia are found to have a high-density component in the innermost layer according to the above analyses. Extremely long-term photometric observations are available for a few SNe Iax (SN 2008ha, Foley et al. 2014; SN 2012Z, McCully et al. 2021), which show slowly decaying light curves even in the extremely late phases ($\geq$1400 d). These observations are consistent with our analysis, and probably support the presence of the inner component. The very slow decay even in such a late phase may disfavor the possibility of homologously expanding inner ejecta as the origin of the inner dense component. However, the luminosity in the very late phase may indeed decrease even more slowly than the radioactive decay, which might require an additional power source, e.g., interaction with circumstellar material (McCully et al. 2021); then it would not provide a strong constraint on the evolution of the optical depth of the inner component. Further observation and analysis covering the full evolution of SNe Iax will help understand their nature.
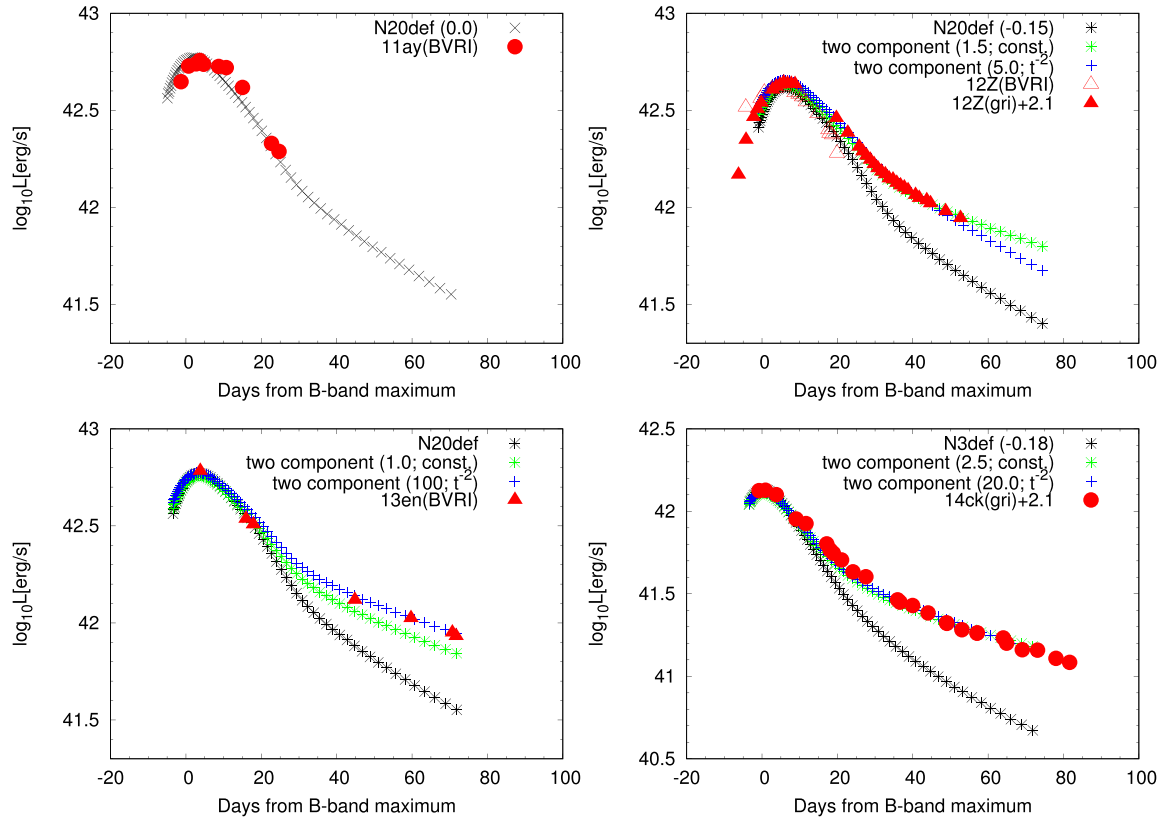
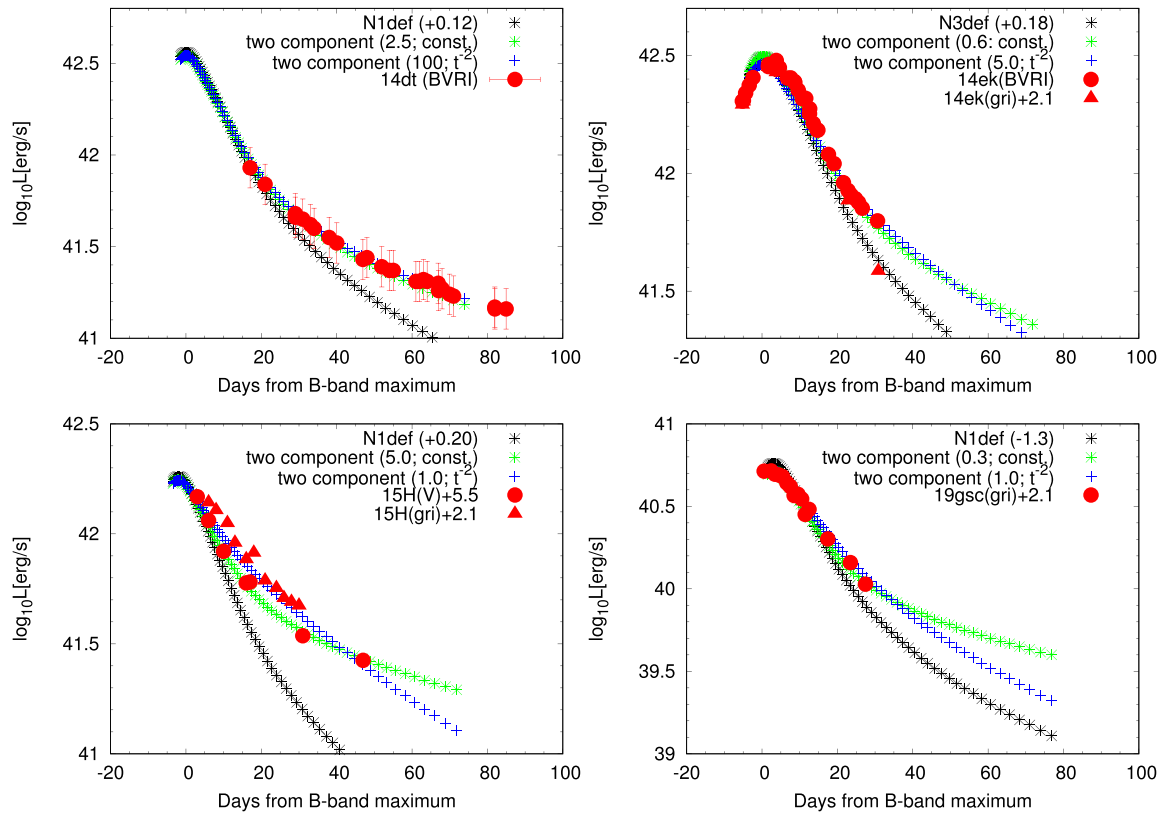**Fig. 15.** As figure 13 but for different SNe Iax. (Color online)

Fig. 16. As figure 13 but for different SNe Iax. (Color online)

Table 6. Data sets of SNe Iax and the properties.

SN	L_{peak} $(10^{42} \, \mathrm{erg \, s^{-1}})$	τ	$[(M_{ej}/M_\odot)^2/E_{51}]_{in}$	$M^{56}Ni_{out}$	$M^{56}Ni_{in}$	Distance (Mpc)	$E(B-V)$ (mag)	Band	References[*]
2002cx	3.2	5.0	1.6	0.007	0.038	104.2	0.034	*BVRI*	1
2005cc	1.1	3.0	0.8	0.084	0.020	37.0	0.0056	*BVRI*	2,3,4,5
2005hk	3.6	3.5	7.9	0.065	0.029	49.2	0.11	*BVRI ugriz*	4,6,7
2008A	5.4	3.5	7.4	0.267	0.030	70.0	0.0427	*BVRI*	8
2008ge	2.5	2.0	2.3	0.175	0.278	16.8	0.0109	*V*	9
2008ha	0.1	1.5	0.8	0.074	0.043	21.3	0.075	*BVRI ugri*	10,11
2009ku	5.0	0.3	0.6	0.278	0.829	370.0	0.0063	*gri*	12
2010ae	0.3	0.1	0.3	0.062	0.072	13.1	0.62	*BV gri*	11
2011ay	6.0	—	—	0.017	—	86.9	0.081	*BVRI*	13
2012Z	4.5	1.5	0.7	0.271	0.122	30.2	0.036	*BVRI ugri*	14,15
2013en	6.3	1.0	14.9	0.266	0.091	66.2	0.5	*BVRI*	16
2014ck	3.2	2.5	3.2	0.083	0.045	24.4	0.48	*gri*	17
2014dt	1.2–1.8	2.5	16.6	—	0.020	14.5	0.02	*BVRI*	18
2014ek	3.2	0.6	0.8	0.071	0.039	99.5	0.054	*BVRI gri*	19
2015H	—	5.0	0.5	0.038	0.049	60.57	0.048	*V gri*	20
2019gsc	0.025	0.3	0.2	0.086	0.100	39.8	0.01	*gri*	21
2019muj	0.5	5.0	16.6	0.047	0.018	31.1	0.023	*BVRI*	22

*References: 1. Li et al. (2003); 2. Ganeshalingam et al. (2010); 3. Silverman et al. (2012); 4. Lennarz, Altmann, and Wiebusch (2012); 5. Foley et al. (2013); 6. Sahu et al. (2008); 7. Holtzman et al. (2008); 8. Hicken et al. (2012); 9. Foley et al. (2010); 10. Foley et al. (2009); 11. Stritzinger et al. (2014); 12. Narayan et al. (2011); 13. Szalai et al. (2015); 14. Stritzinger et al. (2015); 15. Yamanaka et al. (2015); 16. Liu et al. (2015); 17. Tomasella et al. (2016); 18. Kawabata et al. (2018); 19. Li et al. (2018); 20. Magee et al. (2016); 21. Srivastav et al. (2020); 22. This work.

The explosion simulations by Fink et al. (2014) predict the ^{56}Ni masses in the inner and outer layers for a given set of input parameters to characterize the explosion. In table 6 we show the parameters obtained by our fit to the observed light curves. The ^{56}Ni masses required to fit the late-phase light curves are substantially larger than the model predictions. In particular, SNe 2009ku and 2008ge show large discrepancies.

An additional issue is that we do not see a correlation between the properties of the outer ejecta and the inner component expected in the explosion simulations. Figure 17 shows the relationship between the obtained ^{56}Ni mass in the outer layer and that in the inner layer. Fink et al. (2014) predicted that the model with a larger amount of ^{56}Ni in the outer ejecta has less ^{56}Ni mass in the inner layer. However, our results do not follow a clear correlation. This discrepancy indicates that there may still be missing functions in the explosion mechanism of SNe Iax and the origin(s) of their diverse properties that we have not considered in our current analysis.

We also check whether there is a relation between the ejecta mass in the outer layer and the optical depth in the inner component. In the model calculation by Fink et al. (2014), for a smaller explosion energy the bound WD mass becomes larger and the outer ejecta mass becomes smaller. The combination of the larger WD mass and smaller explosion energy likely leads to a larger optical depth of the inner
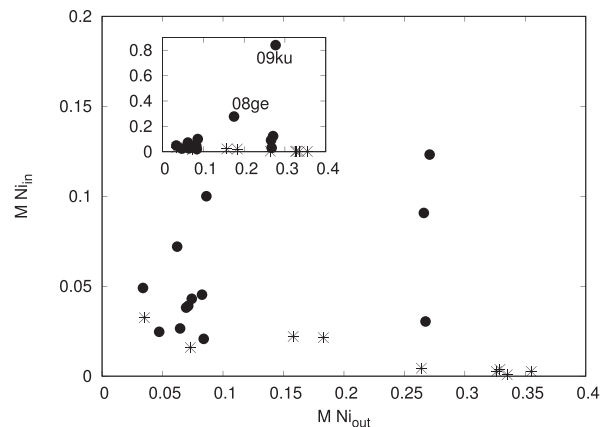
Fig. 17. Relationship between the ^{56}Ni mass in the outer layer and that in the inner layer (filled circles). The asterisk symbols denote the ^{56}Ni masses calculated by Fink et al. (2014).

component along with this scenario, while the detail will be dependent on the specific origin for the inner component. We may anyway expect, at least roughly, an anti-correlation between the outer ejecta mass and the inner optical depth. We show this exercise in figure 18. We do not see a clear relation between the two parameters. Similar to the conclusion reached by the non-correlation between the ^{56}Ni masses in the inner and outer components, the finding here would further indicate that an important function is still missing in our analysis or in our understanding of the nature of SNe Iax.
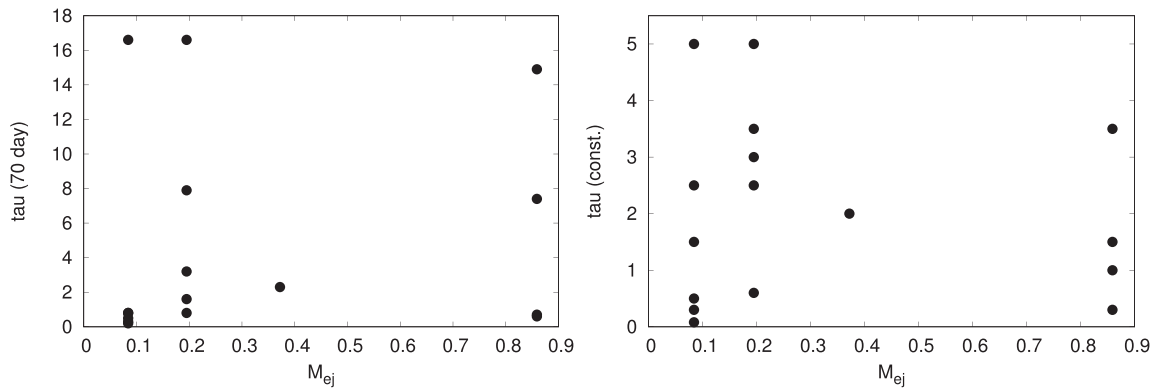
Fig. 18. Relationship between the ejecta mass in the outer layer and the optical depth in the inner component. For the optical depth, two cases are shown: τ = constant (right panel) and $\tau \propto t^{-2}$ (left panel). For the latter case, the optical depth is given at 70 d after the explosion.

5 Conclusions

We have presented a long-term observation of SN 2019muj. Based on the photometric properties of SN 2019muj, it belongs to the intermediate subclass between the bright and subluminous SNe Iax (see also Barna et al. 2021). The spectroscopic features are similar to those of subluminous SNe Iax such as SNe 2008ha and 2010ae, with narrow absorption lines and slow expansion velocity. The similarity between the intermediate and subluminous subclasses in the spectroscopic features is in line with previous work (e.g., Stritzinger et al. 2014). Our long-duration observations covering the epochs up to ∼200 d after the *B*-band maximum show that SN 2019muj exhibits slow evolution of the light curve in the late phase. This behavior is similar to what was previously found for the bright SN Iax 2014dt. Our observational data for SN 2019muj, including the multi-band data from the rising phase, serve as a reference data set for a class of intermediate SNe Iax, given that such well-sampled data are still limited for this class.

We estimated that the ^{56}Ni mass was 0.01–0.03 $M_\odot$, the kinetic energy was ∼(0.02–0.19) × 10^{50} erg, and the ejecta mass was ∼0.16–0.95 $M_\odot$. These values are consistent with the predictions of the weak deflagration model.

The slow evolution in the late phase is best explained by an additional high-density component in the innermost layer. We reproduced the entire bolometric light curves of SN 2019muj and a sample of SNe Iax from the early to late phases by adopting a phenomenological light curve model where we added an inner dense component powered by ^{56}Ni, with the optical depth and ^{56}Ni mass treated as free parameters. The model can explain the light curves of SNe Iax in general, which might support the existence of a high-density component in most, if not all, SNe Iax. The currently available data set is not, however, sufficient to further specify the origin of this inner component; this could be ei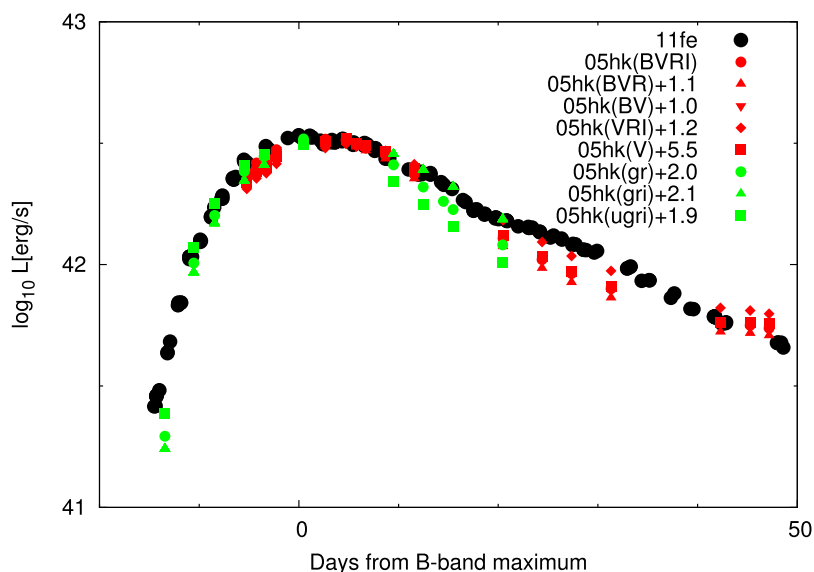ther the remnant WD itself, the slowly moving inner ejecta, or a wind launched from the WD. In any case, the remnant WD would likely create an inner dense component, and thus the present study supports the weak/failed deflagration model.

Our analysis also reveals possible shortcomings of applying the weak deflagration model as it is to the observations of SNe Iax; some important functions may still be missing in the present model. We find no clear correlation between the ^{56}Ni masses in the outer ejecta and in the inner component, which is, however, predicted from the explosion simulations. Similarly, there no relation is found between the outer ejecta mass and the inner optical depth. In addition, the masses of ^{56}Ni to explain the late-time luminosity are found to be generally larger than the model prediction. For the moment, it is not clear if the discrepancy could be remedied by considering the detailed physical processes involved in the evolution of the remnant WD and its radiation. To constrain the nature of the bound WDs and test further the weak deflagration scenario, detailed observations of candidate WDs with an extremely unusual atmospheric composition in the Milky Way (e.g., LP 40-365; Vennes et al. 2017) would be useful.

Fig. 19. Bolometric light curves of SN 2005hk constructed based on the data taken with different combinations of the photometric bands. The different symbols and colors denote the luminosity estimated using the different bands. These light curves are shifted vertically by the amount indicated in the top-right portion of the panel to match the *BVRI* light curve around maximum light. The *BVRI* light curve is assumed to be bolometric, which matches the bolometric light curve of SN 2011fe with an arbitrary shift in the vertical axis (black circles). (Color online)

Appendix. Bolometric light curves of sample SNe Iax

We assume that the *BVRI* light curve of an SN Iax, as obtained by interpolating the SED and integrating the fluxes in the *BVRI* bands, closely follows the bolometric light curve (see subsection 4.2). However, the complete *BVRI* data are not always available, and sometimes different filter systems are used to observe different SNe. We therefore apply the different bolometric corrections to the data obtained with different combinations of the filter set.

To obtain the bolometric correction for the data taken with different filter sets, we use the light curve data of well-observed SN Iax 2005hk, under the assumptions that the bolometric corrections are the same for all SNe Iax and do not evolve with time. First, we constructed the luminosity of SN 2005hk integrated with different sets of the photometric bands. The luminosity obtained is generally smaller than the *BVRI* luminosity, because we only use the data in a limited number of the bands. Then, these light curves obtained for different filter sets are shifted vertically to match the *BVRI* light curve (which is assumed to be the bolometric light curve). The amount of the shift here is taken as the bolometric correction, and this is different for different filter sets.

In figure 19 we compare the bolometric light curves of SN 2005hk estimated for different filter sets as described above. Also shown is the bolometric light curve of SN 2011fe as a cross-check. The bolometric corrections thus obtained for SN 2005hk are used for other SNe Iax, depending on the available filters for individual SNe Iax. The bolometric light curves of a sample of SNe Iax obtained in this manner are shown in figures 20, 21, and 22.

---

[7] ⟨http://www.nhn.ou.edu/ suspect/⟩.
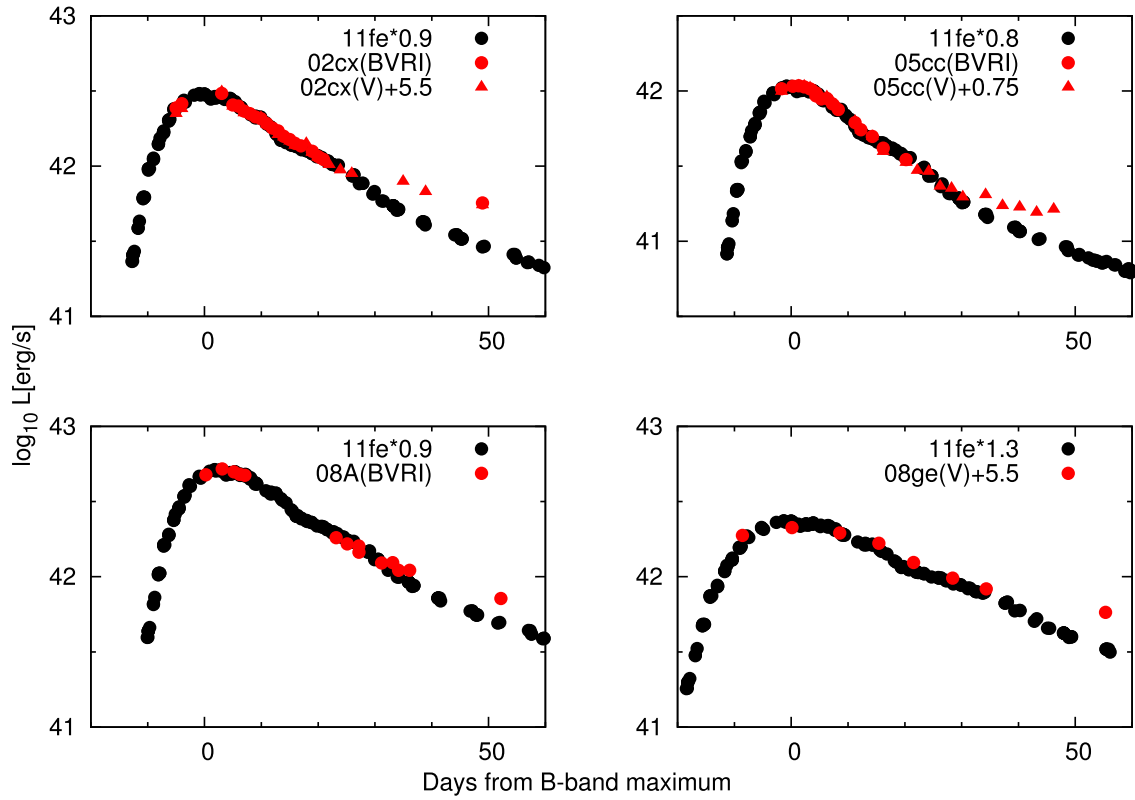
[8] ⟨http://wiserep.weizmann.ac.il/⟩.

Fig. 20. Bolometric light curves of SNe 2002cx (left top), 2005cc (right top), 2008A (left bottom), and 2008ge (right bottom), plotted in the same manner as figure 19. (Color online)
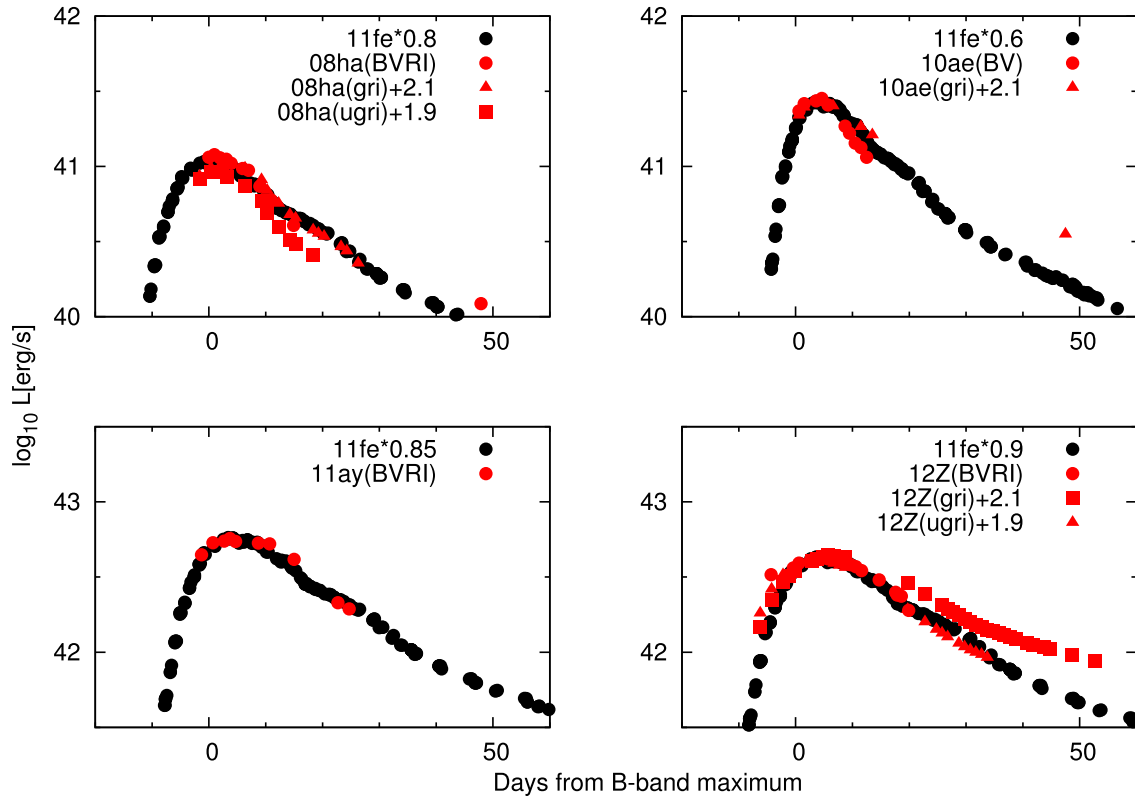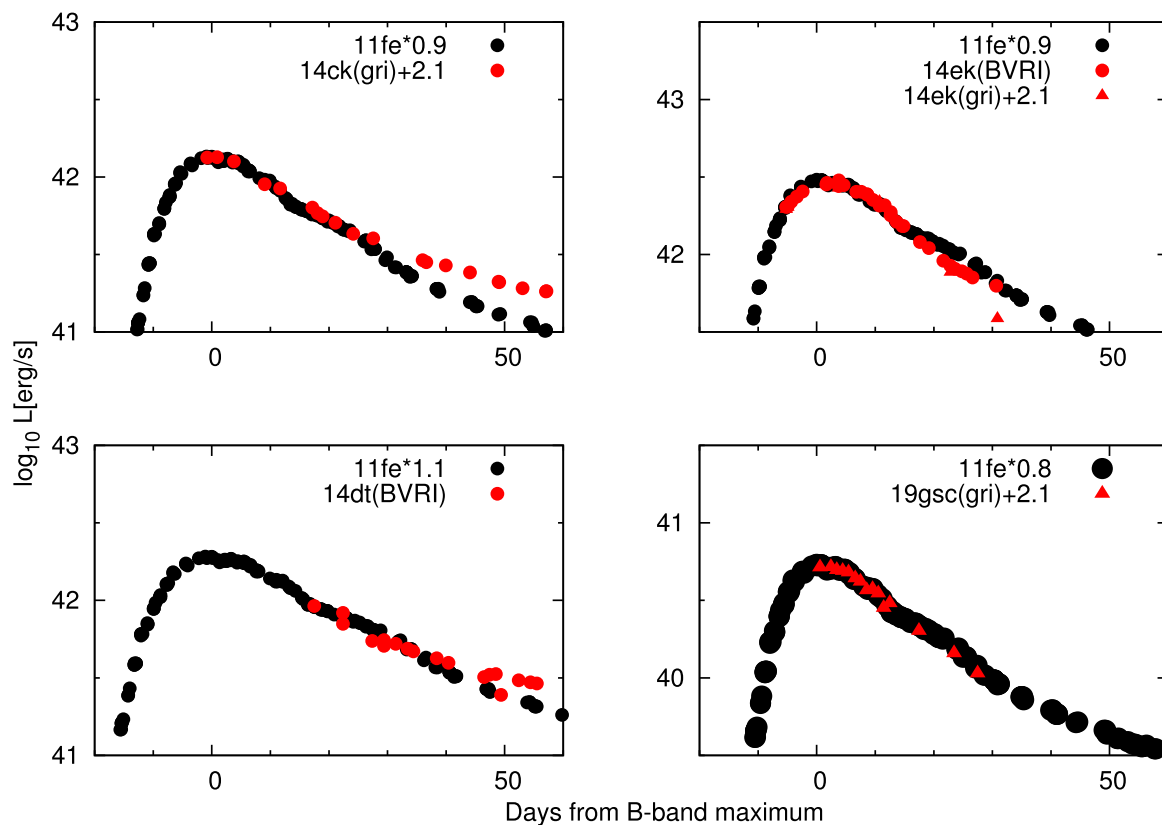
Fig. 21. Bolometric light curves of SNe 2008he (left top), 2010ae (right top), 2011ay (left bottom), and 2012Z (right bottom), plotted in the same manner as figure 19. (Color online)

Fig. 22. Bolometric light curves of SNe 2014ck (left top), 2014ek (right top), and 2014dt (left bottom), plotted in the same manner as figure 19. The open circles for SN 2014dt show the bolometric light curve assuming that the sum of fluxes in the *BVRI*-bands occupied about 60% of the bolometric one. (Color online)

References

Akitaya, H., et al. 2014, in Proc. SPIE, 9147, Ground-Based and Airborne Instrumentation for Astronomy V, ed. S. K. Ramsay et al. (Bellingham, WA: SPIE), 91474O

Arnett, W. D. 1982, ApJ, 253, 785

Barden, S. C., & Armandroff, T. 1995, in Proc. SPIE, 2476, Fiber Optics in Astronomical Applications, ed. S. C. Barden (Bellingham, WA: SPIE), 56

Barden, S. C., Armandroff, T., Muller, G., Rudeen, A. C., Lewis, J., & Groves, L. 1994, in Proc. SPIE, 2198, Instrumentation in Astronomy VIII, ed. D. L. Crawford & E. R. Craine (Bellingham, WA: SPIE), 87

Barna, B., et al. 2021, MNRAS, 501, 1078

Blondin, S., et al. 2012, AJ, 143, 126

Breeveld, A. A., Landsman, W., Holland, S. T., Roming, P., Kuin, N. P. M., & Page, M. J. 2011, in AIP Conf. Proc., 1358, Gamma Ray Bursts 2010, ed. J. E. McEnery et al. (New York: AIP), 373

Brimacombe, J., et al. 2019, Astronomer's Telegram, 13004, 1

Fink, M., et al. 2014, MNRAS, 438, 1762

Foley, R. J., Brown, P. J., Rest, A., Challis, P. J., Kirshner, R. P., & Wood-Vasey, W. M. 2010, ApJL, 708, L61

Foley, R. J., Jha, S. W., Pan, Y.-C., Zheng, W. K., Bildsten, L., Filippenko, A. V., & Kasen, D. 2016, MNRAS, 461, 433

Foley, R. J., McCully, C., Jha, S. W., Bildsten, L., Fong, W.-f., Narayan, G., Rest, A., & Stritzinger, M. D. 2014, ApJ, 792, 29

Foley, R. J., et al. 2009, AJ, 138, 376

Foley, R. J., et al. 2013, ApJ, 767, 57

Fox, O. D., et al. 2016, ApJ, 816, L13

Ganeshalingam, M., et al. 2010, ApJS, 190, 418

Hayden, B. T., et al. 2010, ApJ, 712, 350

Hicken, M., et al. 2009, ApJ, 700, 331

Hicken, M., et al. 2012, ApJS, 200, 12

Hiramatsu, D., Arcavi, I., Burke, J., Howell, D. A., McCully, C., Pellegrino, C., & Valenti, S. 2019, Global SN Project Transient Classification Report for 2019-08-07, No. 2019-1442

Hoeflich, P., & Khokhlov, A. 1996, ApJ, 457, 500

Hoeflich, P., Khokhlov, A. M., & Wheeler, J. C. 1995, ApJ, 444, 831

Holtzman, J. A., et al. 2008, AJ, 136, 2306

Jha, S., Branch, D., Chornock, R., Foley, R. J., Li, W., Swift, B. J., Casebeer, D., & Filippenko, A. V. 2006, AJ, 132, 189

Jha, S. W. 2017, in Handbook of Supernovae, ed. A. W. Alsabti & P. Murdin (Cham: Springer), 375

Jiang, J.-a., et al. 2020, ApJ, 892, 25

Jordan, G. C. I., Perets, H. B., Fisher, R. T., & van Rossum, D. R. 2012, ApJ, 761, L23

Kashikawa, N., et al. 2002, PASJ, 54, 819

Kawabata, K. S., et al. 2008, in Proc. SPIE, 7014, Ground-Based and Airborne Instrumentation for Astronomy II, ed. I. S. McLean & M. M. Casali (Bellingham, WA: SPIE), 70144L

Kawabata, M., et al. 2018, PASJ, 70, 111

Kawabata, M., et al. 2020, ApJ, 893, 143

Kromer, M., et al. 2013, MNRAS, 429, 2287

Kromer, M., et al. 2015, MNRAS, 450, 3045

Kurita, M., et al. 2020, PASJ, 72, 48

Landolt, A. U. 1992, AJ, 104, 340

Lennarz, D., Altmann, D., & Wiebusch, C. 2012, A&A, 538, A120

Li, L., et al. 2018, MNRAS, 478, 4575

Li, W., et al. 2003, PASP, 115, 453

Liu, Z.-W., et al. 2015, MNRAS, 452, 838

McClelland, C. M., et al. 2010, ApJ, 720, 704

McCully, C., et al. 2021, ApJ submitted (arXiv:2106.04602)

Maeda, K., Mazzali, P. A., Deng, J., Nomoto, K., Yoshii, Y., Tomita, H., & Kobayashi, Y. 2003, ApJ, 593, 931

Maeda, K., & Terada, Y. 2016, Int. J. Mod. Phys. D, 25, 1630024

Magee, M. R., et al. 2016, A&A, 589, A89

Matsubayashi, K., et al. 2019, PASJ, 71, 102

Moriya, T., Tominaga, N., Tanaka, M., Nomoto, K., Sauer, D. N., Mazzali, P. A., Maeda, K., & Suzuki, T. 2010, ApJ, 719, 1445

Nagayama, T., et al. 2003, in Proc. SPIE, 4841, Instrument Design and Performance for Optical/Infrared Ground-Based Telescopes, ed. M. Iye & A. F. M. Moorwood (Bellingham, WA: SPIE), 459

Narayan, G., et al. 2011, ApJ, 731, L11

Nomoto, K., Sugimoto, D., & Neo, S. 1976, Ap&SS, 39, L37

Nugent, P. E., et al. 2011, Nature, 480, 344

Pereira, R., et al. 2013, A&A, 554, A27

Perlmutter, S., et al. 1999, ApJ, 517, 565

Persson, S. E., Murphy, D. C., Krzeminski, W., Roth, M., & Rieke, M. J. 1998, AJ, 116, 2475

Phillips, M. M. 1993, ApJL, 413, L105

Phillips, M. M., et al. 2007, PASP, 119, 360

Richardson, D., Thomas, R. C., Casebeer, D., Blankenship, Z., Ratowt, S., Baron, E., & Branch, D. 2001, BAAS, 199, 84.08

Riess, A. G., et al. 1998, AJ, 116, 1009

Riess, A. G., et al. 1999, AJ, 118, 2675

Sahu, D. K., et al. 2008, ApJ, 680, 580

Schlafly, E. F., & Finkbeiner, D. P. 2011, ApJ, 737, 103

Shappee, B., et al. 2014, AAS Meeting Abstracts, #223, 236.03

Silverman, J. M., et al. 2012, MNRAS, 425, 1789

Singh, A., Srivastav, S., Kumar, B., Anupama, G. C., & Sahu, D. K. 2018, MNRAS, 480, 2475

Srivastav, S., et al. 2020, ApJ, 892, L24

Stritzinger, M., et al. 2002, AJ, 124, 2100

Stritzinger, M., & Leibundgut, B. 2005, A&A, 431, 423

Stritzinger, M. D., et al. 2014, A&A, 561, A146

Stritzinger, M. D., et al. 2015, A&A, 573, A2

Szalai, T., et al. 2015, MNRAS, 453, 2103

Tomasella, L., et al. 2016, MNRAS, 459, 1018

Valenti, S., et al. 2009, Nature, 459, 674

van Dokkum, P. G. 2001, PASP, 113, 1420

van Dokkum, P. G., Bloom, J., & Tewes, M. 2012, Astrophysics Source Code Library, ascl:1207.005

Vennes, S., Nemeth, P., Kawka, A., Thorstensen, J. R., Khalack, V., Ferrario, L., & Alper, E. H. 2017, Science, 357, 680

Yamanaka, M., et al. 2015, ApJ, 806, 191

Yaron, O., & Gal-Yam, A. 2012, PASP, 124, 668

Yoshida, M. 2005, J. Korean Astron. Soc., 38, 117

Zhang, K., et al. 2016, ApJ, 820, 67